Escola de Camins
Escola Tècnica Superior d'Enginyeria de Camins, Canals i Ports
UPC BARCELONATECH

TREBALL FINAL DE MÀSTER

A continuous damage model to mimic sharp cracks in quasi-brittle materials

Treball realitzat per:
Montserrat Casado-Antolin

Dirigit per:
Antonio Rodríguez-Ferran

Màster en:
Enginyeria de Camins, Canals i Ports

Barcelona, juny de 2018

Departament d'Enginyeria Civil i Ambiental

Abstract

A continuous damage model
to mimic sharp cracks in quasi-brittle materials

Montserrat Casado-Antolín

Continuous gradient models have been proved to provide accurate results in the simulation of the failure process of quasi-brittle materials –concrete or rocks, for instance. These approaches are suitable to describe the early stages of material degradation, consisting on damage inception and propagation. However, regarding the modelling of cracks, they can only provide a smeared representation.

The goal of this thesis is to present a new contribution to better characterise the representation of discontinuities working with a continuous gradient-enhanced damage model. The main concern of this work is to mimic sharp cracks. With this purpose, cracks are defined considering two main features: having a zero load-carrying capacity and exhibiting zero non-local interaction.

Regarding the first feature, an artificial stiffness is used without altering the constitutive equation. Considering the softening characterisation of quasi-brittle materials, this means that damage is allowed to reach its maximum value without producing the traditional singularity problems. Hence, forces are able to reach a value of zero, which corresponds to a zero load-carrying capacity.

As for the second feature, in the context of gradient models, avoiding non-local interaction means that no diffusion of strains should be exhibited once the material is fully damaged. In this direction, this work proposes a new formulation of the regularisation equation consisting on transient gradient activity, with the purpose of avoiding the strain spreading.

First, a binary gradient activity is developed, where diffusion is active and constant until the moment when the specimen is fully degraded, when it is switched off. However, the gradient activity control function is not differentiable when damage is maximum, in $d = 1$, which causes convergence problems.

Second, in order to overcome this issue, a gradual gradient activity formulation is proposed. In this case, the gradient activity control function decreases as damage increases and is differentiable in all the domain. Both approaches allow to avoid the unrealistic damage plateau exhibited in constant gradient activity models.

Furthermore, the regularisation capabilities of the new formulations are verified and the contribution of the control activity function shape parameter p and the diffusion parameter or characteristic length ℓ are analysed. Appropriate values need to be used in order to obtain accurate results. Finally, the performance of these techniques are illustrated with one- and two-dimensional examples.

Graphical abstract

A continuous damage model to mimic sharp cracks in quasi-brittle materials

Montserrat Casado-Antolín

ORIGINAL CRACK REPRESENTATION

Residual artificial stiffness

$$\mathbf{K} = \int (1-d)\mathbf{B}^{\mathrm{T}}\mathbf{C}\mathbf{B}\mathrm{d}x$$

$$d \leq 0.9999$$

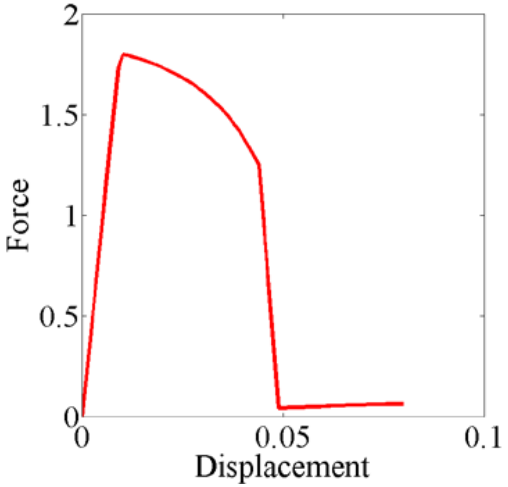

Residual load-carrying capacity

Constant gradient activity

$$\widetilde{\mathbf{u}} - \ell^2 \nabla^2 \widetilde{\mathbf{u}} = \mathbf{u}$$

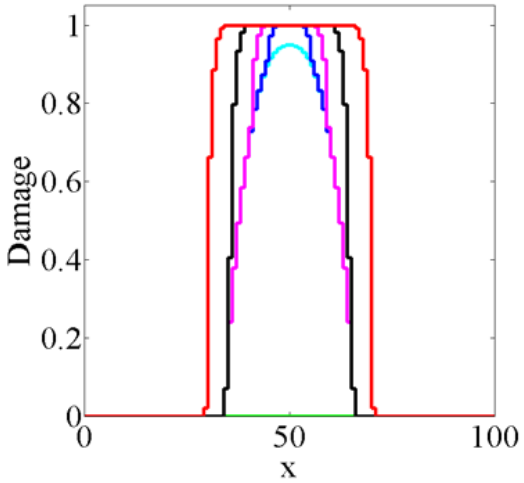

Damage plateau

PROPOSED CRACK REPRESENTATION

Artificial stiffness

$$\mathbf{K} = \int k_{\mathrm{art}}\mathbf{B}^{\mathrm{T}}\mathbf{C}\mathbf{B}\mathrm{d}x$$

$$k_{\mathrm{art}} = \max\left(10^{-q}, (1-d)\right)$$

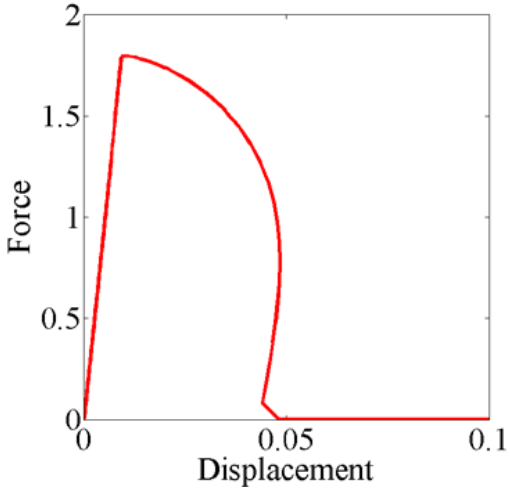

Zero load-carrying capacity

Transient gradient activity

$$\widetilde{\mathbf{u}} - \nabla \cdot \left(\ell^2(1-d^p) \cdot \nabla \widetilde{\mathbf{u}}\right) = \mathbf{u}$$

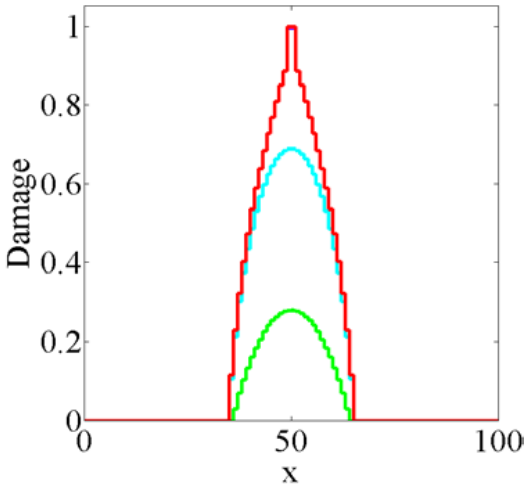

Zero non-local interaction

Acknowledgements

The work presented in this dissertation would have never been possible without the support of my advisor, Antonio Rodríguez. Antonio, many thanks for your guidance all along the development of this thesis and for your permanent willingness to help me, no matter the distance. Thanks also for your support all these years and above all, for your motivation and encouragement to always improve and aim high. Many thanks as well to Elena Tamayo-Mas for sharing her PhD codes.

I would like to thank Jordi for his skills to aim beyond the expected. Many thanks for the amazing experiences we have lived together and for keep sharing that ambition to become skilled engineers with me.

I would also like to express my gratitude to my parents and my wonderful brother, who have always supported my decisions and even travelled halfway across the world just to share an incredible experience with me. *Family, gràcies pel suport que m'heu donat aquests anys, per escoltar-me i animar-me. Gràcies per inculcar-me els valors de l'esforç i la constància desde petita, no hauria arribat fins aquí sense vosaltres.*

Finally, to my grandma, who has been and always will be an inspiration to all of us.

Contents

List of Figures

List of Tables

Chapter 1

Introduction

1.1 Motivation

In engineering, the understanding of materials response is of vital importance in order to design and predict the behaviour of any structure or machine. Particularly, the degradation of materials, which will eventually produce failure, is a key issue. Quasi-brittle materials –such as concrete, rocks and some ceramics– exhibit a softening structural response, that is, their stiffness decreases until failure is reached. This degradation of the material is attributed to the formation of micro-cracks, which eventually develop and lead to macro-cracks and the ultimate loss of load-carrying capacity.

In civil engineering, cracks in quasi-brittle materials may appear in many occasions. It can be exhibited in any structure built in concrete such as bridges, dams, floor slabs, pillars; but also on rocks, as in hydraulic fracturing or in carbon sequestration.

The understanding of quasi-brittle failure can be acquired by carrying out both experimental and numerical tests. Although laboratory experiments allow to study real material structures, numerical simulations exhibit several advantages. Numerical tests can be easily repeated and allow the analysis of full-scale structures for long time periods and at a lower cost. However, one must not discard experimental tests since they are complementary to numerical ones.

The study of fracture in quasi-brittle materials is traditionally tackled with one of these

two numerical approaches: (a) damage mechanics, where a continuous model is used to study the first stages of the failure process, like damage inception and propagation; or (b) fracture mechanics, where a discontinuous model is used to analyse the last stages of the failure process, dealing with cracks and material separation, see Sukumar et al. (2015). Furthermore, in recent years, combined continuous-discontinuous models have been developed incorporating treats of both approaches with the objective of simulating the whole failure process, as presented by Tamayo-Mas and Rodríguez-Ferran (2015).

Both continuous and discontinuous models have advantages and disadvantages, being appropriate depending on the needs of the problem. On the one hand, continuous models require a less complex computational technology, which generally results in less computational cost, but provide a smeared representation of the crack. On the other hand, discontinuous models allow to explicitly represent the discontinuity, which is needed in certain applications such as introducing the effect of a fluid pressure inside the crack, but require a more sophisticated finite-element technology.

In particular, continuous models have been proved to be accurate enough to represent discontinuities. The objective of this dissertation is to present a continuous approach which is able to simulate a realistic sharp –rather than smeared– discontinuity. To this end, two main treats are examined regarding the crack definition: having a zero load-carrying capacity and exhibiting zero non-local interaction.

1.2 Goals and layout of this thesis

The objective of this thesis is to develop a technique that allows to mimic a sharp discontinuity within a continuous setting. To this end, two goals have been conceived:

1. **To propose an adjustment that allows to have zero load-carrying capacity.** The techniques generally used in gradient models in order to avoid the singularity of the stiffness matrix cause an artificial residual load-carrying capacity once the material is fully degraded. In Chapter 3, these techniques are discussed and a method to allow the stresses to be zero once the material is fully damaged is proposed.

2. **To propose an adjustment that allows to have zero non-local interaction.** Once the specimen is fully degraded and the crack is formed, the presence of non-local interaction along the discontinuity is not possible. In the context of gradient

models, this means that no diffusion of strains should be exhibited. In order to avoid this physically unrealistic phenomenon, two modifications on the gradient model are proposed:

1. **Binary gradient activity**. In Chapter 3, a formulation based on a binary transient diffusion is presented. In this approach, the diffusion is set constant until the specimen is fully degraded, when it is set to zero. The regularisation capabilities are tested and the influence of the diffusion parameter or characteristic length ℓ are discussed. In order to verify the performance of this approach, a uniaxial tension test and a shear band test are performed.
2. **Gradual gradient activity**. In Chapter 4, a formulation based on gradual transient diffusion is developed. In this approach, diffusion gradually decreases as damage increases, reaching a value of zero when damage is maximum. In this case, the influence of the characteristic length ℓ and the gradient control function shape parameter p are discussed. Besides, the regularisation capabilities are also examined. Finally, the model is validated with one- and two-dimensional numerical simulations.

Chapter 2

State of the art

This chapter provides an overview of the main numerical strategies developed to simulate quasi-brittle fracture, such as in concrete or rocks. The advantages and disadvantages of some of the most employed computational methods for fracture are discussed. Moreover, the main difficulties and the techniques arisen to solve them are outlined.

Traditionally, failure of quasi-brittle materials is treated following two approaches: damage mechanics, based on continuous models and fracture mechanics, based on discontinuous ones. Regarding the modelling of a crack, continuous models work with a smeared representation of the crack, conceived as an area with high strain concentration. Discontinuous models, instead, deal with an explicit representation, provided by the displacement jump.

In Sections 2.1 and 2.2, continuous models and discontinuous models are discussed, respectively. Finally, combined continuous-discontinuous approaches are reviewed in Section 2.3.

2.1 Continuous models

The first stages of failure, consisting on damage inception and propagation, are usually simulated with continuous models. These approaches deal with the failure phenomena from the point of view of damage mechanics, considering a continuously differentiable displacement field. Hence, a continuous strain field is derived. Continuous models de-

scribe fracture as a process of strain localisation and damage growth, where cracks are represented by continuum regions that have lost their local load-carrying capacity. The constitutive laws required to describe quasi-brittle materials must present strain softening. This behaviour is represented by a stress-strain law which is nearly linear up to the peak stress and decreases after reaching it.

Classical continuum theories work with local models, i.e., the stress at a point only depends on the strain history at that point. However, the results provided by local models exhibit a pathological mesh-dependence, leading to unrealistic results. With the purpose of overcoming this sensitivity to discretisation parameters –such as mesh size– several solutions have been proposed in the literature, Rabczuk (2013).

Crack-band approach

The crack-band model –also called *fracture energy approach* or *mesh-adjusted softening modulus*–, presented by Bažant and Oh (1983), consists on adjusting the post-peak slope of the stress-strain curve by means of the element size. Its main advantage is that the structure of the finite element code does not require major changes since the formulation remains local. Nevertheless, as discussed by Jirásek and Bauer (2012), the criterion for estimating the width of the crack band is not straightforward. In fact, it depends on several parameters such as the element type, the element shape and the direction of the crack band with respect to the mesh edges.

Regularised formulations

These models prevent strain localisation into an arbitrarily small volume by means of an additional material parameter: the characteristic length ℓ. Nevertheless, the quantitative determination of this parameter is a complex issue since it cannot be directly measured and may be only inferred by inverse analysis of test results. These models include non-local integral and gradient-enriched formulations.

In *integral-type* models, an internal variable Y is replaced by its non-local counterpart $\widetilde{Y}$, computed by weighted averaging of Y. Thus, the stress at a given point does not only depend on the strain at that point but also on the strain of the considered neighbourhood. For a detailed overview of non-local formulations that provide an appropriate description of the complete failure process, see Bažant and Jirásek (2002).

Gradient-type non-local models, see de Borst et al. (1995) and Peerlings et al. (1998), set a differential –rather than integral– relation between local and non-local variables. Indeed, a partial differential equation (PDE) relating these local and non-local variables is added to the system. The choice of appropiate boundary conditions required by this PDE is discussed by Tamayo-Mas (2013).

In this dissertation, a gradient-enriched formulation is used to regularise softening. Moreover, non-locality is introduced at the level of displacements, as presented by Rodríguez-Ferran et al. (2005).

2.2 Discontinuous models

Discontinuous models are suitable to simulate the last stages of the failure process, consisting on macro-cracks formation and material separation. These approaches deal with failure from the point of view of fracture mechanics. They consider a discontinuous displacement field, i.e., a displacement field with jumps or strong discontinuities. Hence, the strain field has, on the one hand, a regular part computed by standard differentiation of the displacement field, and on the other hand, a singular part considering the contributions of the displacement jump. Therefore, the crack can be represented explicitly.

Several approaches to deal with displacement discontinuities have been discussed in the literature and provide a reliable simulation of failure processes, see Simo et al. (1993), Simo and Oliver (1994) and Armero and Garikipati (1996). Despite that, standard finite element approximations cannot capture strong discontinuities. Some computational methods are outlined in this section, for a detailed review, see Jirásek and Bauer (2012) and Rabczuk (2013).

Remeshing

In remeshing methods, the standard finite element method (FEM) is used. Nevertheless, the element edges –in 2D– or faces –in 3D– must be aligned with the crack and the nodes located on these edges or faces must be doubled. Due to this, the finite element mesh must be reconstructed each time the crack propagates, which becomes a computationally inefficient process.

Embedded discontinuities

This approach, inspired by Ortiz et al. (1987) and Belytschko et al. (1988) and reviewed by Jirásek (2000), captures displacement jumps by enriching the approximation of the displacement field with additional functions. The enrichment is elemental, a feature that requires reduced changes in finite element codes. Besides, the need for remeshing when propagation occurs is avoided.

eXtended Finite Element Method (X-FEM)

X-FEM is widely used to simulate the presence of cracks in a finite element framework, see Belytschko and Black (1999) and Moës et al. (1999). It is based on the partition of unity concept, which is considered to decompose the displacement field into a continuous and a discontinuous part. That is, the standard finite element interpolation of the displacement field is enriched with discontinuous functions. The enrichment employed in this technique is nodal.

In addition to the above-mentioned strategies, approaches of a different nature exist as well to simulate fracture. *Meshless methods*, Belytschko et al. (1996) and Nguyen et al. (2008), efficiently model evolving discontinuities due to the the absence of a mesh. In *phase-field methods*, cracks are assumed to propagate along the minimum energy path, see Bourdin et al. (2000) and Francfort and Marigo (1998).

2.3 Continuous-discontinuous models

Continuous models are suitable to describe the early stages of the failure process, between the undamaged state and macroscopic crack initiation. Once the crack is introduced, discontinuous models are appropriate to simulate the last stages, incorporating into the model discontinuous displacement fields. Then, a combination of both approaches has arisen to achieve a better characterisation of the entire failure process: continuous-discontinuous models, see for instance Mazars and Pijaudier-Cabot (1996), Jirásek and Zimmermann (2001), Wells et al. (2002), Simone et al. (2003) and Comi et al. (2007).

The continuous-discontinuous technique can be summarised in several stages:

1. **Continuous regime.** For the first stages of the failure process, non-local continu-

ous models are employed. This allows to capture damage inception and propagation.

2. **Transition.** Once the transition –or switching– criterion is fulfilled, a discontinuity is introduced. In order to carry out an appropriate transition, some issues must be examined:

   - **Switching criterion.** The transition from a continuous to a discontinuous model is carried out when the damage field reaches a critical value d_{crit}. This critical value determines whether traction-free cracks are introduced (the material is fully degraded) or cohesive cracks are inserted (otherwise). This is one of the most accepted switching criteria; however, alternative methods are also employed such as setting the critical value directly to strains, Jirásek and Zimmermann (2001), or stresses.
   - **Crack path definition.** Due to the fact that linear elastic fracture mechanics cannot be employed in a regularised bulk, the crack path cannot be analytically derived. Therefore, location and propagation of the crack are generally assumed to be known before-hand. However, several new contributions address this issue. For instance, Tamayo-Mas and Rodríguez-Ferran (2015) propose a geometric criterion to determine the crack path, the θ-simplified medial axis (θ-SMA), which locates the crack through the middle of the damage bulk.
   - **Energy consistency.** When switching from the continuous model to the discontinuous one, the energy not yet dissipated by the bulk has to be transferred to the cohesive crack. The computation of this energy is not straightforward and the extension to a multidimensional setting needs further improvements. In contrast to cohesive cracks, another option is simulating traction-free cracks, where no energetic considerations need to be taken into account.

3. **Discontinuous regime.** The final stages of the failure process, explicit macroscopic cracks and material separation, are modelled by means of discontinuous models.

A first contribution of coupled models is presented by Mazars and Pijaudier-Cabot (1996), where thermodynamic relationships between the two classical theories are discussed. Jirásek and Zimmermann (2001) propose to combine smeared cracks for early stages of material degradation with embedded discontinuities for stages where strain reaches a

critical value. Simone et al. (2003) combines an implicit gradient-enhanced continuum damage model with a traction-free crack. In Tamayo-Mas and Rodríguez-Ferran (2013), the whole process is tackled with a continuous-discontinuous approach which considers an implicit gradient-enhanced damage model based on smooth displacements to drive damage evolution, X-FEM to introduce the crack and the θ-SMA to propagate it.

Chapter 3

Continuous damage model with binary gradient activity

The aim of this chapter is to propose a technique that allows to simulate a sharp discontinuity within a continuous setting. In order to achieve so, two main features need to be reproduced once the material is fully damaged: (1) a zero load-carrying capacity and (2) zero non-local interaction.

First, a review of continuous gradient models is exposed in Section 3.1. Then, the two main features are discussed: in Section 3.2, an adjustment which considers an artificial residual stiffness without altering the constitutive equation is developed to avoid spurious load-carrying capacity and in Section 3.3, binary transient gradient activity is analysed to avoid diffusion. Finally, in Section 3.4 a numerical example is carried out in order to validate the model proposed.

3.1 Introduction to gradient activity

Regularisation

Classical continuum theories typically exhibit pathological mesh-dependence, which provides physically unrealistic results. This means that the finite element size determines the response of the material. In order to avoid this behaviour, non-locality needs to be introduced. In this work, the gradient-enhanced model based on smoothed displacements

presented by Rodríguez-Ferran et al. (2005) is used. The regularisation equation shows that non-locality is incorporated at the level of displacements,

$$\widetilde{\mathbf{u}}\,(\mathbf{x},t) - \ell^2\nabla^2\widetilde{\mathbf{u}}\,(\mathbf{x},t) = \mathbf{u}\,(\mathbf{x},t) \tag{3.1}$$

where $\widetilde{\mathbf{u}}$ are the non-local or smoothed displacements, $\mathbf{u}$ the local displacements and ℓ the characteristic length of the non-local damage model (or diffusion parameter).

This model computes the non-local displacements $\widetilde{\mathbf{u}}$ from the local displacements $\mathbf{u}$ as the solution of the second-order PDE (3.1). Indeed, the regularisation PDE is in this case a diffusion-reaction equation. To solve it, appropriate boundary conditions for the smoothed displacement field $\widetilde{\mathbf{u}}$ must be imposed. As discussed in Tamayo-Mas (2013), the combined boundary conditions

$$\left.\begin{array}{rcl} \widetilde{\mathbf{u}}\cdot\mathbf{n} & = & \mathbf{u}\cdot\mathbf{n} \\ \mathbf{n}\cdot\nabla\widetilde{\mathbf{u}}\cdot\mathbf{t} & = & \mathbf{n}\cdot\nabla\mathbf{u}\cdot\mathbf{t} \end{array}\right\} \text{on } \partial\Omega \tag{3.2}$$

where $\mathbf{n}$ denotes the unit normal to Ω and $\mathbf{t}$ is the tangent vector such that $\{\mathbf{n},\mathbf{t}\}$ form an orthonormal basis for $\mathbb{R}^2$; provide the required properties for the regularisation equation.

With this, Dirichlet boundary conditions are prescribed for the normal component of the displacement field and non-homogeneous Neumann boundary conditions are imposed for the tangential components. They are prescribed using the Lagrange multipliers method. In Appendix A, the treatment of the mechanical and the regularisation boundary conditions is discussed.

Gradient damage model

In order to characterise the material, the constitutive equation is expressed as

$$\boldsymbol{\sigma}(\boldsymbol{\varepsilon},\widetilde{\boldsymbol{\varepsilon}}) = \big[1 - d(\widetilde{\boldsymbol{\varepsilon}})\big]\,\mathbf{C} : \boldsymbol{\varepsilon} \tag{3.3}$$

where $\boldsymbol{\sigma}$ is the Cauchy stress tensor, $\boldsymbol{\varepsilon}$ and $\widetilde{\boldsymbol{\varepsilon}}$ the local and non-local (or smoothed) small strain tensors respectively, $\mathbf{C}$ the tensor of elastic moduli and d the damage parameter.

Note that local and smoothed strains are computed from the local and smoothed displacements $\mathbf{u}$ and $\widetilde{\mathbf{u}}$, respectively,

$$\begin{aligned} \boldsymbol{\varepsilon}(\mathbf{x},t) &= \nabla^s\mathbf{u}(\mathbf{x},t) \\ \widetilde{\boldsymbol{\varepsilon}}(\mathbf{x},t) &= \nabla^s\widetilde{\mathbf{u}}(\mathbf{x},t) \end{aligned} \tag{3.4}$$

where ∇^s is the symmetrised gradient.

It can be observed in Eq. (3.3), that the loss of stiffness $\mathbf{C}$ is driven by means of the damage parameter d, which has values from 0 (undamaged material) to 1 (fully degraded material). The evolution of the non-decreasing damage parameter d is driven by the non-local state variable κ

$$d(\kappa) = \begin{cases} 0 & \text{for} \quad \kappa \leq \kappa_i \\ f(\kappa) & \text{for} \quad \kappa_i \leq \kappa \leq \kappa_u \\ 1 & \text{for} \quad \kappa \geq \kappa_u \end{cases} \tag{3.5}$$

or

$$d(\kappa) = \begin{cases} 0 & \text{for} \quad \kappa < \kappa_i \\ f(\kappa) & \text{for} \quad \kappa \geq \kappa_i \end{cases} \tag{3.6}$$

where κ is considered a history variable since it is defined as the historical maximum non-local state variable Y

$$\kappa = \max_{\tau \leq t} \; Y(\widetilde{\boldsymbol{\varepsilon}}) \tag{3.7}$$

The damage evolution law $d(\kappa)$ can be either linear, a power law (3.5) or exponential (3.6), as depicted in Figure 3.1.

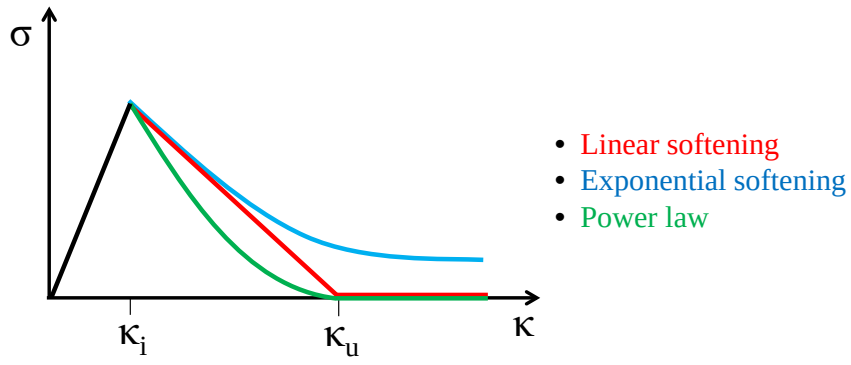

Figure 3.1: Different damage evolution laws.

3.2 Zero load-carrying capacity

The objective of this section is to simulate a zero load-carrying capacity once the material is fully degraded. This zero load-carrying capacity is achieved when the stresses $\boldsymbol{\sigma}$ in the constitutive equation (3.3) are zero. In order to obtain so, the damage parameter d must reach its maximum value $d = 1$, once $\kappa = \kappa_u$ in linear or power law softening or once κ is sufficiently large in exponential softening.

As a consequence of the damage parameter reaching a value of $d = 1$, a zero secant stiffness is obtained. This is due to the fact that a softening damage model is used, being the stiffness matrix defined as

$$\mathbf{K} = \int (1 - d)\mathbf{B}^{\mathrm{T}}\mathbf{C}\mathbf{B}\mathrm{d}x \tag{3.8}$$

with $\mathbf{B}$ the matrix of shape functions derivatives.

However, in computational engineering, it is vital to avoid the singularity of the stiffness matrix $\mathbf{K}$ so that it is possible to solve the system of equations $\mathbf{K}\mathbf{x} = \mathbf{f}$.

In order to avoid this singularity, the constitutive equation is traditionally modified to leave a residual stiffness. Generally, gradient models set an upper bound on the damage parameter, slightly lower than 1 (e.g. $d_{\max} = 0.9999$). Taking into consideration the definition of the stiffness matrix in Eq. (3.8), it can be observed that preventing the damage parameter d from reaching 1, allows to avoid the singularity of the secant stiffness matrix, since the term $(1 - d)$ will never become zero.

Another way to avoid singularity problems is to work with a damage evolution law consisting on an exponential softening model that includes a residual strength, like the one depicted in Figure 3.1. Again, the objective is to avoid damage from reaching its maximum real value $d = 1$, that is, total degradation of the material is not permitted.

These techniques produce an artificial residual stiffness, which causes an undesired residual load-carrying capacity. Since the computation is not aborted because of singularity problems, displacements -and therefore, strains- continue growing. Considering the constitutive equation (3.3), this increasing strain causes also an increase on the stresses. As a consequence, a residual load-carrying capacity is observed. Figure 3.2 shows a one-dimensional uniaxial tension test where this residual load-carrying capacity is observed once the unloading is finished.

In order to avoid the residual load-carrying capacity and to allow a total degradation of the material, an artificial residual stiffness will be used, without altering the constitutive equation. To do so, no upper bound on the damage parameter d will be imposed or no residual strength will be included on the damage law. Instead, the damage parameter will be allowed to reach its maximum value $d = 1$. In order to avoid the secant stiffness matrix to become singular, it will be defined as

$$\mathbf{K} = \int k_{\mathrm{art}}\mathbf{B}^{\mathrm{T}}\mathbf{C}\mathbf{B}\mathrm{d}x \tag{3.9}$$

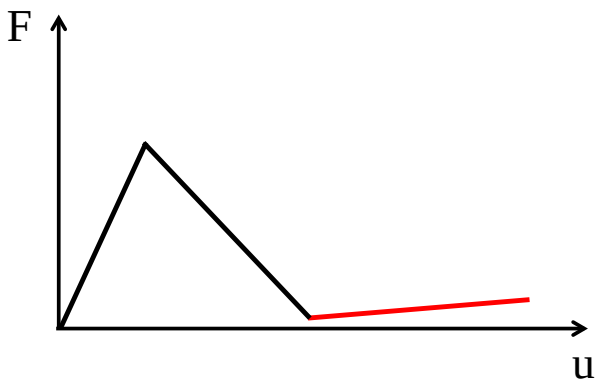

Figure 3.2: Residual load-carrying capacity, in red.

with

$$k_{\text{art}} = \max\left(10^{-q}, (1-d)\right). \tag{3.10}$$

Thus, once the damage parameter is close to $d = 1$, the term $(1 - d)$ will be substituted by 10^{-q} but no restrictions will be applied to d, which will be able to continue growing until its maximum value. Since the damage parameter is not limited, the constitutive equation (3.3) is not altered and stresses will be able to reach zero once the material is fully degraded ($d = 1$), so no spurious load-carrying capacity will be obtained.

Note that the value of q must be chosen such that it is sufficiently large to provide realistic results but sufficiently low to avoid singularity in the stiffness matrix.

3.2.1 Numerical example

A uniaxial tension test is carried out in order to explore this alternative way to work with a residual artificial stiffness without affecting the constitutive equation. A bar with a centred weakened part as depicted in Fig. 3.3 is analysed. Its left end is blocked and a prescribed displacement is applied on the right one.

The dimensionless geometric and material parameters used in this test are summarised in Table 3.1. Regarding the damage evolution law, linear softening is used. A 10% reduction in Young's modulus is applied to the weakened part to cause localisation. By setting Poisson's ratio to $\nu = 0$, the lateral effect can be neglected and the test can be considered a one-dimensional problem.

The problem is discretised with a mesh of 100×1 two-dimensional quadrilateral finite

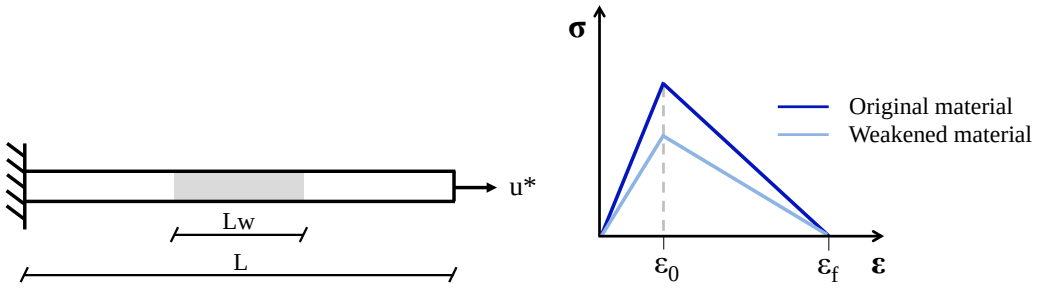

Figure 3.3: Problem statement for the uniaxial tension test.

Meaning	Symbol	Value
Length of the bar	L	100
Cross-section of the bar	A	1
Length of the weakened part	L_{W}	30
Young's modulus	E	20 000
Young's modulus for weakened part	E_{W}	18 000
Damage threshold	κ_i	10^{-4}
Final strain	κ_f	1.25×10^{-2}

Table 3.1: Uniaxial tension test: dimensionless geometric and material parameters.

elements. Regarding regularisation, the test is run for a characteristic length of $\ell = 1$. In order to introduce an artificial residual stiffness as defined in Eq. (3.2) and avoid singularity, a value of $q = 4$ is used. Therefore,

$$k_{\mathrm{art}} = \max\left(10^{-4}, (1-d)\right). \tag{3.11}$$

Both the mechanical and the regularisation boundary conditions described in Figure 3.3 and Eq. (3.2), respectively, are prescribed using the Lagrange multipliers method, see Appendix A for details. Arc-length control is used in order to capture the snap-back of the force-displacement curve. This way, one will be able to track the real response of the material.

The results of the simulation can be observed in Figure 3.4. The force-displacement response in Figure 3.4(a) shows that no residual load carrying capacity is obtained, being the value of the forces zero once the unloading has been carried out and the piece is fully degraded (state E). For some significant steps in the loading process, specified on the force-displacement curve, the damage field along the bar is exhibited in Figure 3.4(b).

Damage is zero on the elastic branch (state A) and grows once the damage threshold κ_i is reached (states B, C and D). Indeed, it can be observed how damage is successfully allowed to reach its maximum value $d = 1$ from state E on. Hence, stresses are able to reach $\sigma = 0$, which corresponds to a fully-damaged material behaviour when the bar is separated into two independent parts.

In spite of being able to successfully avoid the spurious reloading, an unrealistic damage plateau of value $d = 1$ is observed once the material is fully degraded. In fact, it can be observed that the curves of state E and F are not coincident, as it would be expected since the bar is divided into two independent parts from state E on, and damage should no longer evolve. This unrealistic broadening of the damage field will be treated in Section 3.3.

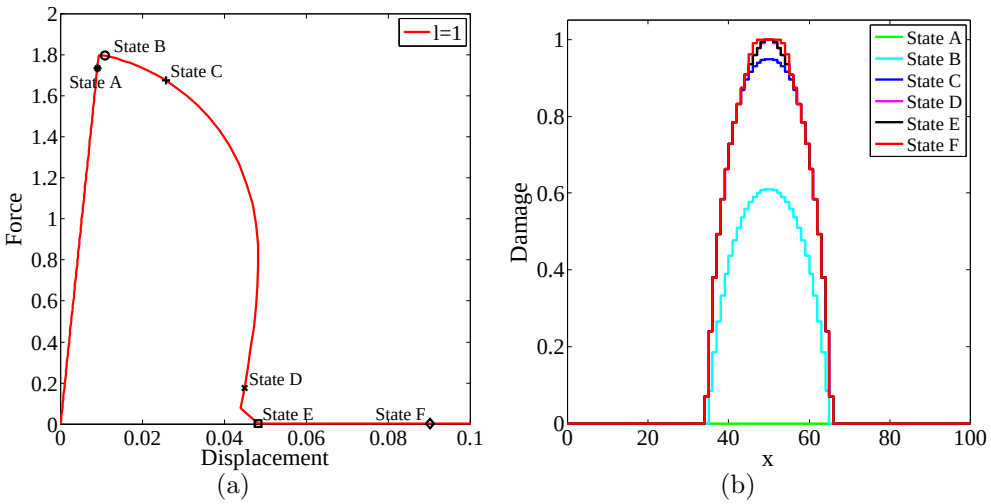

Figure 3.4: Results for the uniaxial test ($\ell = 1$): (a) force-displacement response and (b) damage distribution.

In order to explore the effect on convergence that the proposed adjustment may produce on the stiffness matrix, Figure 3.5 shows plots of convergence for the significant points specified in Figure 3.4(a).

In the elastic branch (state A), only one iteration is needed since a linear problem needs to be solved. In the softening branch, where damage starts to appear (states B, C and D), a non-linear problem needs to be solved. The technique used to solve it is the Newton-Raphson method, so quadratic convergence is observed. Once the damage reaches its maximum value, the artificial residual stiffness is activated and quadratic convergence is lost (states E and F). This is due to the fact that this artificial residual stiffness prevents

the secant stiffness matrix from being fully consistent with the constitutive equation. However, convergence is obtained rapidly, so it is a small price to pay in order to remove the undesired residual load carrying-capacity.

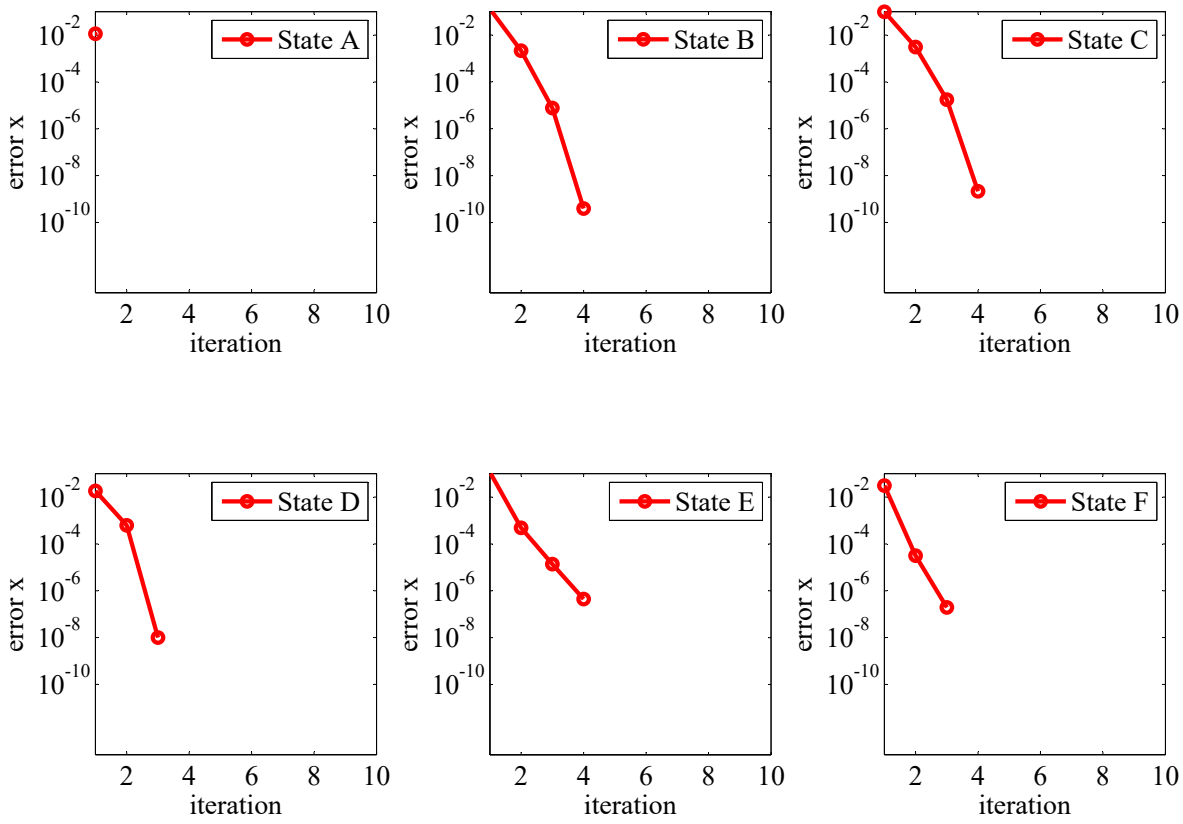

Figure 3.5: Convergence history for load steps A to F, see Figure 3.4(a).

3.3 Zero non-local interaction

In this section, transient gradient activity will be discussed with the aim of dealing with diffusion and avoid the non-physical damage broadening observed in the uniaxial tension test.

As commented in Section 3.1, the model is regularised in order to avoid pathological mesh dependence. Considering the PDE in Eq. (3.1), the characteristic length ℓ of the model consists on a diffusion parameter. In previous sections, diffusion has been set constant during the simulation. However, it is not realistic that once the specimen is fully degraded ($d = 1$), diffusion ℓ continues on.

In order to explore this unrealistic behaviour, the uniaxial simulation of Section 3.2.1 is studied. Several damage fields have been plotted for loading steps after state E, i.e., for loading steps where the bar is already separated in two parts. The results obtained are shown in Figure 3.6(a), where a damage plateau of value $d = 1$ can be observed on the points surrounding the weakened part. The additional diffusion of strains once the material is fully damaged shown in Figure 3.6(b) causes this increasing broadening of the damage field once the bar is divided into two independent parts.

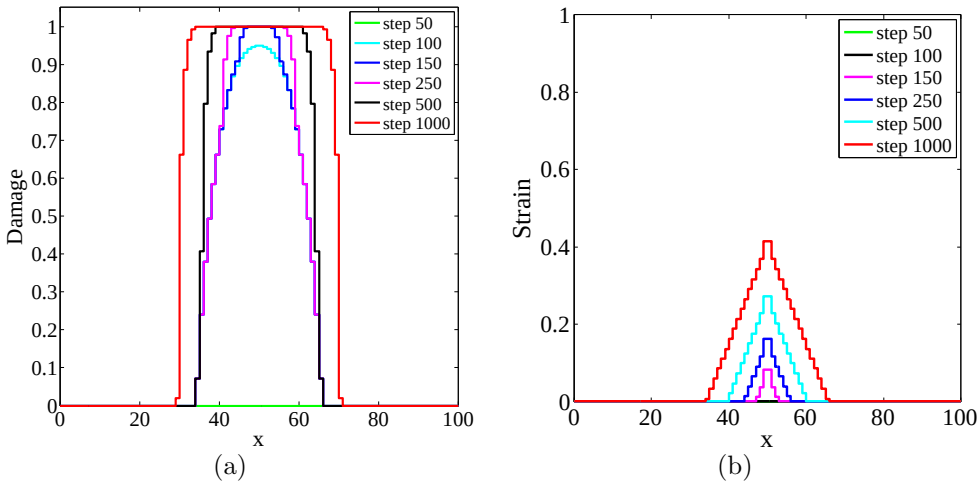

Figure 3.6: (a) Damage broadening and (b) strains diffusion for the uniaxial test once the bar is fully damaged.

In order to avoid this unrealistic damage broadening, an elemental switching off of the diffusion parameter is carried out: once the damage parameter reaches its maximum value $d = 1$ on a finite element, diffusion is set to zero $\ell = 0$ in that element. Hence, the regularisation equation (3.1) reads now

$$\widetilde{\mathbf{u}}\,(\mathbf{x},t) - g(d)\ell^2\nabla^2\widetilde{\mathbf{u}}\,(\mathbf{x},t) = \mathbf{u}\,(\mathbf{x},t) \tag{3.12}$$

with $g(d)$ the gradient activity control function defined as

$$g(d) = \begin{cases} 1 & \text{if} \quad d < 1 \\ 0 & \text{if} \quad d = 1 \end{cases} \tag{3.13}$$

This binary gradient activity is depicted in Figure 3.7. The uniaxial simulation is run including this new definition of the regularisation equation. The resulting damage distribution is shown in Figure 3.8. Note how the damage plateau of value $d = 1$ observed in Figure 3.6(a) is no longer exhibited and only the point where the bar is broken has

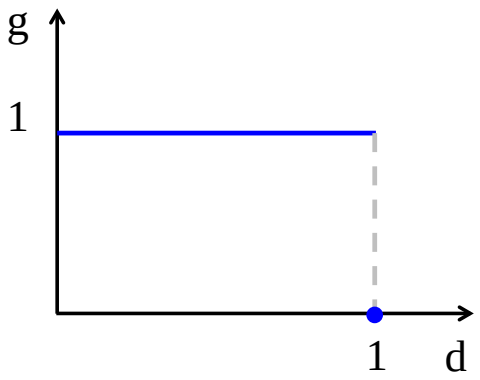

Figure 3.7: Binary transient gradient activity function.

maximum damage (Figure 3.8(b)). Indeed, once damage reaches its maximum value, the same damage distribution is observed for all the following steps. Moreover, the same force-displacement response as in the simulation without switching off is obtained, so no undesired alterations have been produced on the material behaviour. In addition, profiles for the strains and the displacements are also presented. It can be observed how on the weakened part of the bar the strain grows as the simulation continues and on the undamaged parts it goes back to zero. Besides, once the bar is fully damaged (state E) a narrower distribution of strains is exhibited in Figure 3.8(c) than in Figure 3.6(b), where diffusion was not switched off. Thus, no undesired damage plateau is produced. The displacement field has the expected behaviour, exhibiting a steeper slope on the weakened part of the bar than on the original one.

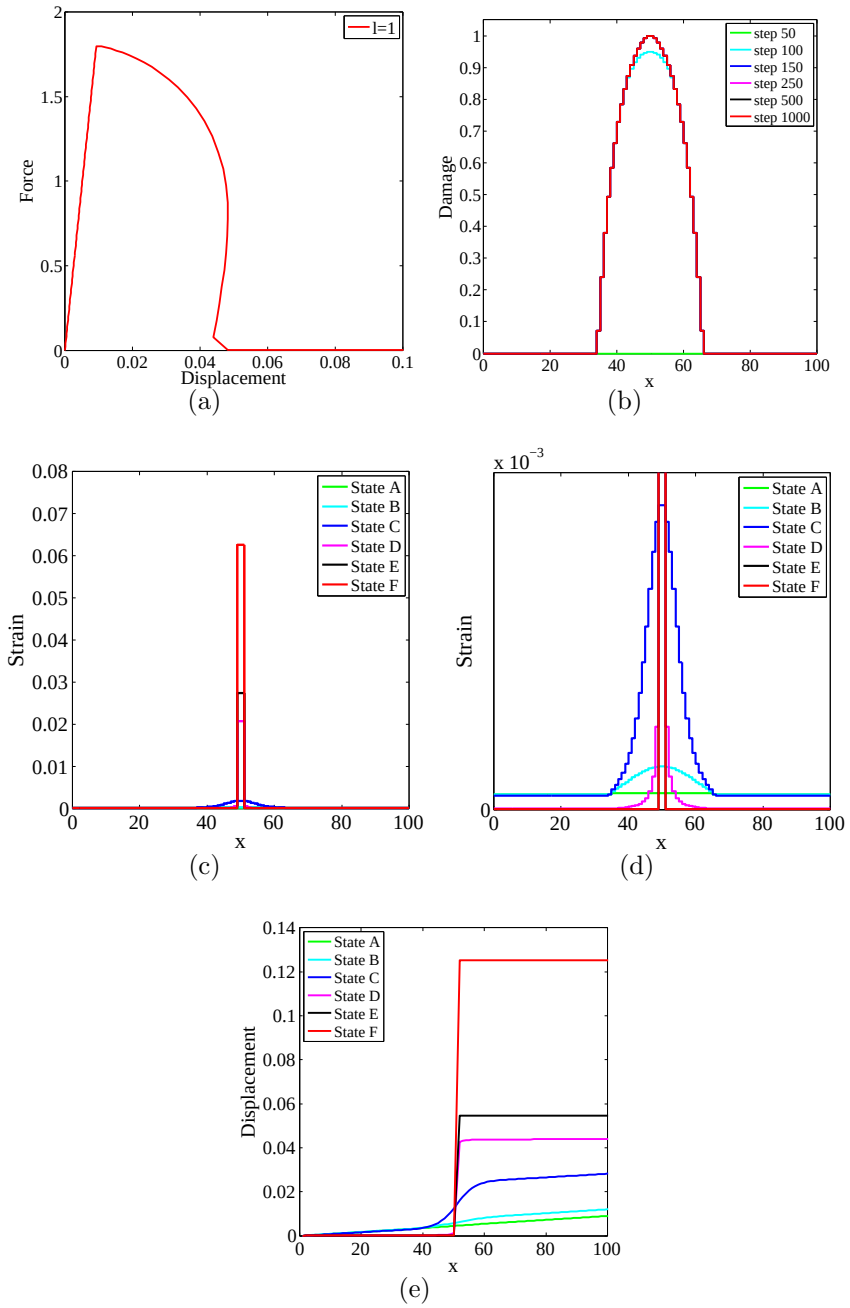

Figure 3.8: Results for the uniaxial test ($\ell = 1$) switching off diffusion once the material is fully degraded:(a) force-displacement response, (b) damage distribution, (c) and (d) strain distribution and (e) displacement profiles.

It is important to remark that switching off diffusion ℓ when the material is fully degraded does not produce any negative effect on regularisation. This is due to the fact that when damage starts to grow, diffusion is on and it is not turned to zero until the crack is formed. Figure 3.9 shows how the same damage distribution is obtained for different finite-element

discretisations of the bar, which means that the results obtained do not depend on the finite-element size.

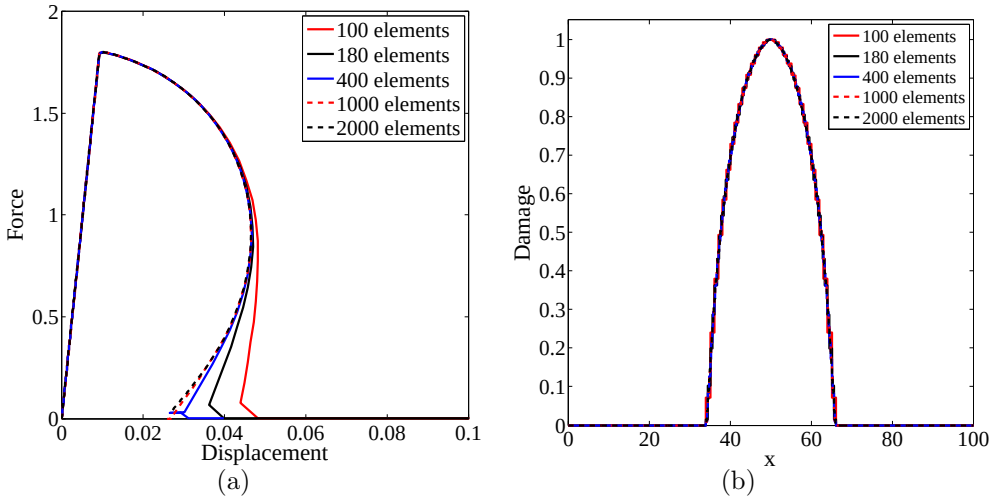

Figure 3.9: (a) Force-displacement response and (b) damage field for different number of elements.

Finally, the same simulation has been carried out increasing the value of diffusion to $\ell = 2$. The same geometrical and material parameters as in Section 3.2.1 have been used, as well as the same mechanical and regularisation boundary conditions. Again, a mesh of 100×1 two-dimensional finite elements and a value of $q = 4$ for the artificial stiffness parameter have been used.

The effect of higher diffusion can be observed on the results in Figure 3.10. Wider distributions are exhibited for the force-displacement response and for the damage and the strain distributions.

Note how for both simulations, with $\ell = 1$ and $\ell = 2$, the two objectives of the proposed technique have been fulfilled: (1) thanks to incorporating artificial stiffness only on the stiffness matrix without altering the constitutive equation, no undesired reloading is observed once the material is fully degraded and (2) by working with a transient diffusion, switched off when damage is maximum, no unrealistic damage broadening is exhibited after the piece is divided into two independent parts. Besides, with these two improvements, the gradient-enhanced model is still mesh-independent.

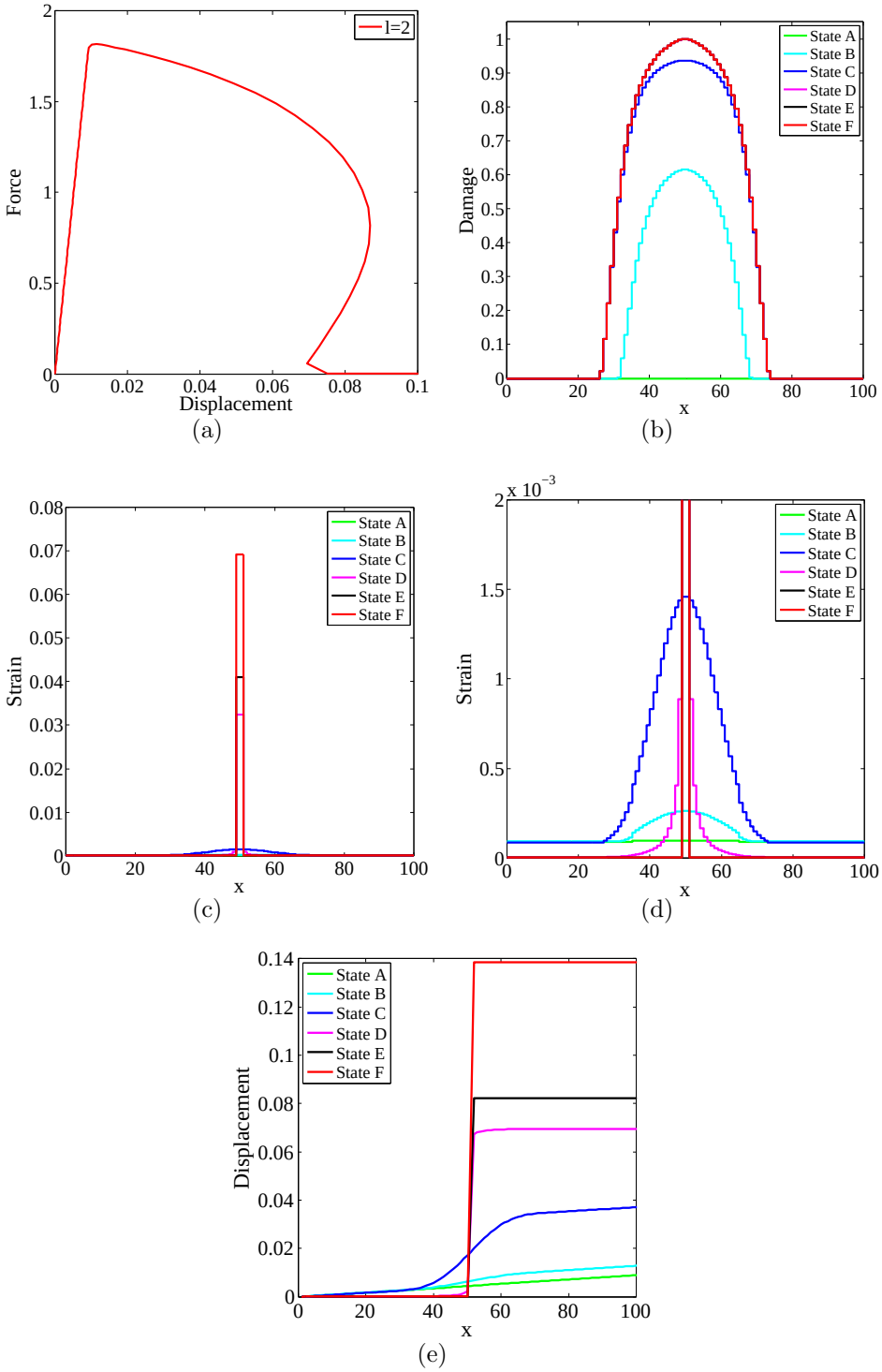

Figure 3.10: Results for the uniaxial test ($\ell = 2$) switching off diffusion once the material is fully degraded: (a) force-displacement response, (b) damage distribution, (c) and (d) strain distribution and (e) displacement profiles.

After these simulations, it can be stated that the proposed adjustments for non-local damage models are suitable for effectively representing a discontinuity in a continuous setting. In the following section, this technique will be validated with a more complex two-dimensional problem.

3.4 Shear band test

In this section, a two-dimensional numerical shear test is carried out. A tensile load is applied to the specimen, with the aim of obtaining a shear band. A corner of the specimen is weakened in order to trigger localisation, as depicted in Figure 3.11. Note how due to geometrical and loading conditions, symmetry can be applied to the problem.

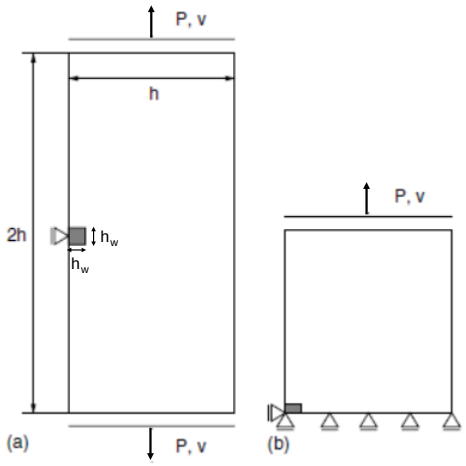

Figure 3.11: Shear test: problem statement. Adapted from Simone et al. (2004).

The dimensionless geometric and material parameters are summarised in Table 3.2. In this case, Poisson's ratio is set to $\nu = 0.2$. The weakening of the corner is carried out by using a lower damage threshold κ_i, instead of reducing the Young's modulus E.

The damage model used is the modified von Mises model, so the equivalent state variable Y is computed as

$$Y = \frac{1}{1+\nu}\sqrt{3J_2} \tag{3.14}$$

where J_2 is the second invariant of the deviatoric strain tensor.

Meaning	Symbol	Value
Width	h	60
Side	t	1
Width of weakened corner	h_W	6
Young's modulus	E	20 000
Damage threshold	κ_i	10^{-4}
Damage threshold of weakened corner	κ_{iW}	0.5×10^{-4}
Residual strength parameter	α	1
Post-peak slope	β	400
Poisson's ratio	ν	0.2

Table 3.2: Shear test: dimensionless geometric and material parameters.

For this test, an exponential damage evolution law is considered.

$$d(\kappa) = 1 - \frac{\kappa_i}{\kappa}\Big[1 - \alpha + \alpha \exp\big(-\beta(\kappa - \kappa_i)\big)\Big] \tag{3.15}$$

where α is the parameter of residual strength and β the post-peak slope or softening stiffness. Note that as the α parameter used is $\alpha = 1$, no residual strength is considered since the damage parameter will be able to reach $d(\kappa) = 1$:

$$d(\kappa) = 1 - \frac{\kappa_i}{\kappa} \exp\big(-\beta(\kappa - \kappa_i)\big) \tag{3.16}$$

Both the mechanical and the regularisation boundary conditions are prescribed using the Lagrange multipliers method, see Appendix A for details.

In order to solve this non-linear problem, Newton-Raphson method is used. Note that arc-length control is used to run the simulation. The problem is discretised with an unstructured mesh of 1576 quadrilateral finite elements, see Figure 3.12. The size of the smallest elements is 1 length unit. Regarding regularisation, a characteristic length of $\ell = 1$ is used. A stiffness parameter of $q = 4$ is used in order to introduce an artificial residual stiffness without altering the constitutive equation, see Eq. (3.2).

The results obtained are shown in Figures 3.13 and 3.14. The force-displacement response shows that there is no need to work with an exponential softening law with residual strength: thanks to the artificial stiffness added with k_{art} in Eq. (3.2), no spurious load-carrying capacity is obtained since the constitutive equation has not been modified.

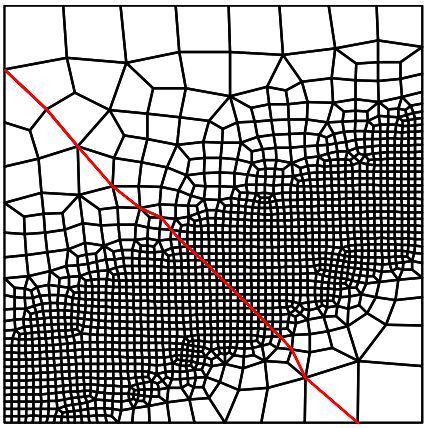

Figure 3.12: Finite element mesh and cross-section for the shear test.

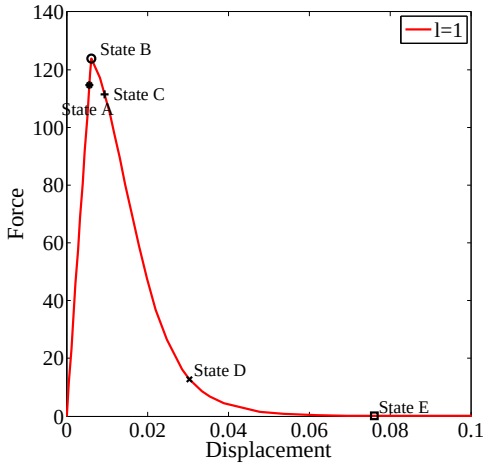

Figure 3.13: Shear test: force-displacement response.

The damage distribution is plotted for the significant points in the loading process specified in Figure 3.13. In order to have a more illustrative representation along the specimen discontinuity, the damage field along the cross-section depicted in Figure 3.12 is shown as well.

It can be observed how damage inception occurs in the weakened corner of the specimen (states A and B) and propagates along the shear band. Since no threshold has been applied to the damage parameter, it is allowed to reach its maximum value, $d = 1$, as it is shown for state E.

Effect of the characteristic length ℓ

The model will be now validated for three cases with the same softening stiffness, repre-

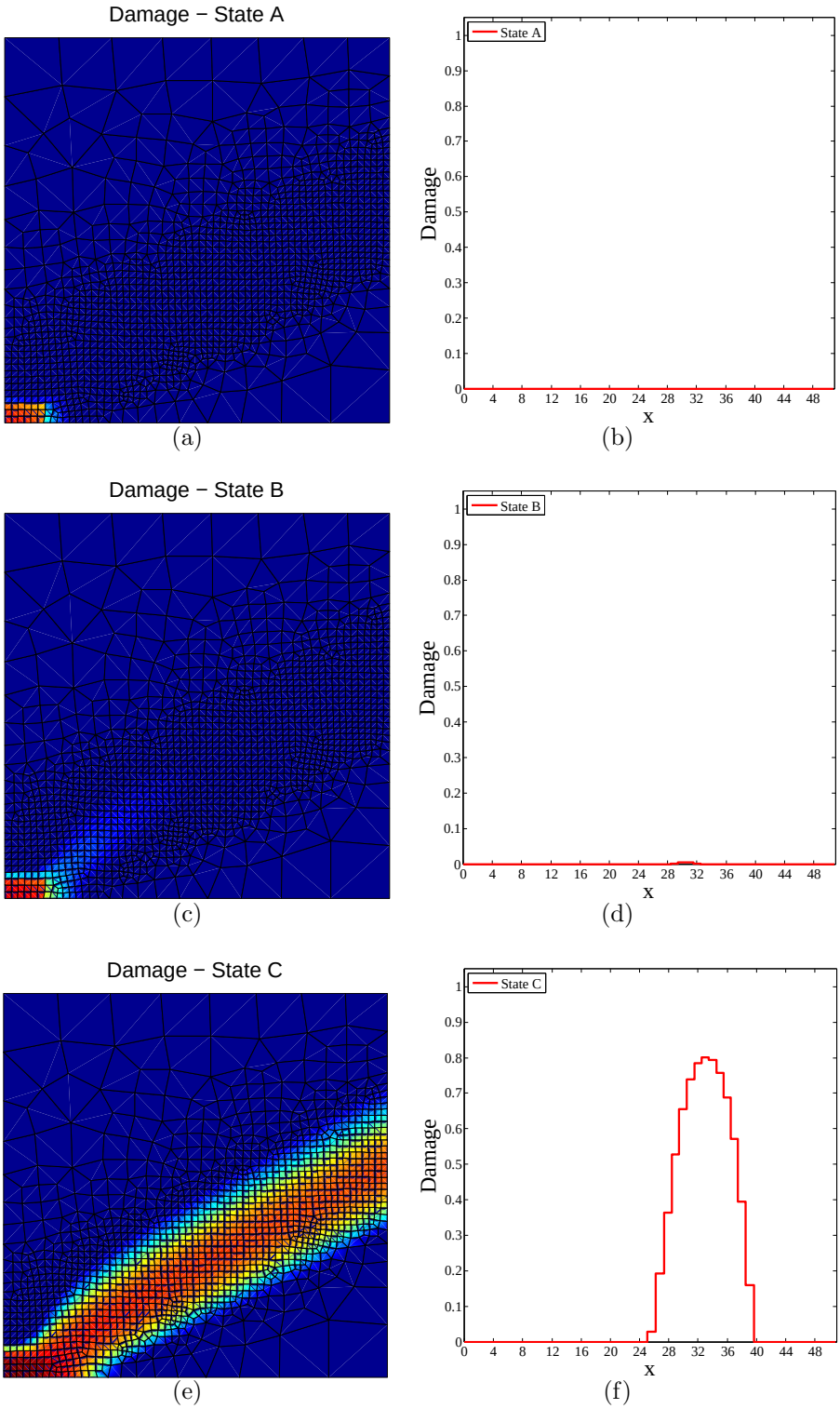

Figure 3.14: Shear test, damage field for (a), (c), (e) the whole specimen and for (b), (d), (f) the cross-section in Figure 3.12; for states A, B and C.

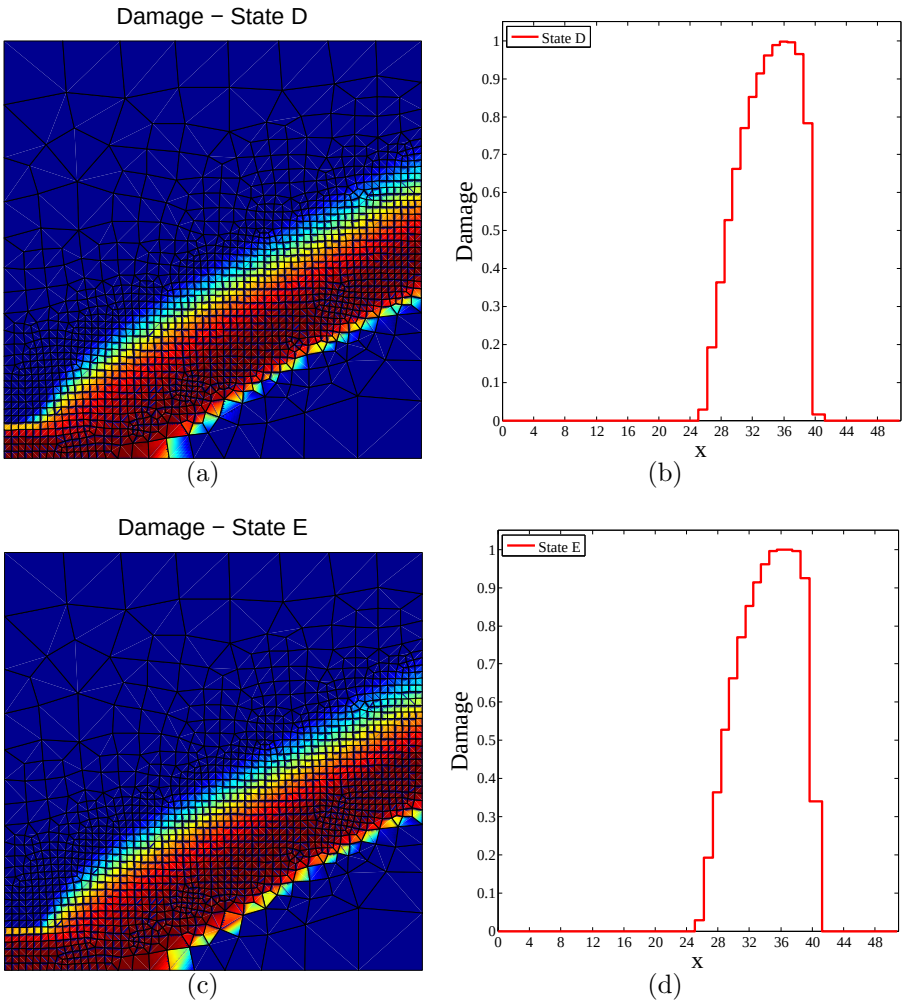

Figure 3.15: Shear test: damage field for (a), (c) the whole specimen and for (b), (d) the cross-section in Figure 3.12; for states D and E.

sented by the post-peak slope parameter β, and different values of characteristic length ℓ. Starting from the reference case in Table 3.2 (case A), a lower value for ℓ is set in case B and a greater value in case C, see Table 3.3.

	Length ℓ	Post-peak slope β
Case A	1	400
Case B	$\sqrt{\frac{1}{2}}$	400
Case C	$\sqrt{2}$	400

Table 3.3: Shear test: cases with different values for ℓ.

The force-displacement responses obtained are shown in Figure 3.16. It can be observed that although all three specimens have the same post-peak slope, a lower characteristic length provides a more brittle material (case B) and the opposite occurs with a higher characteristic length (case C). The diffusion of damage is controlled by this characteristic length ℓ. Figure 3.17 shows the damage fields for the same load steps for the three cases. As expected, the higher ℓ is, the wider the damage field.

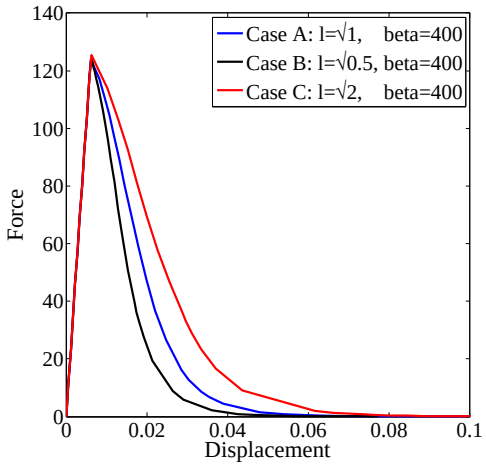

Figure 3.16: Shear test: force-displacement response for different characteristic lengths.

It is also interesting to discuss how the behaviour of the material is controlled by both the characteristic length ℓ and the post-peak slope β. The shear test is simulated for three materials with different values of ℓ and β, see Table 3.4. Starting from the reference case in Table 3.2 (case A), both ℓ and β are increased in case B and decreased in case C.

	Length ℓ	Post-peak slope β	$\ell/\beta^{\frac{3}{2}}$
Case A	1	400	$1.25 \cdot 10^{-4}$
Case B	$\sqrt{2}$	500	$1.26 \cdot 10^{-4}$
Case C	$\sqrt{\frac{1}{2}}$	300	$1.36 \cdot 10^{-4}$

Table 3.4: Shear test: cases with different parameters ℓ and β.

Figure 3.18 shows the force-displacement response of these simulations. It can be observed how all three materials exhibit very similar responses, even though they have different post-peak slope parameters. This is due to the fact that ℓ and β work in a combined way. As presented by Mestre-Bellido (2016), these two parameters are related by means of the relation $\ell/\beta^{\frac{3}{2}}$, which has very similar values for the three cases (Table 3.4).

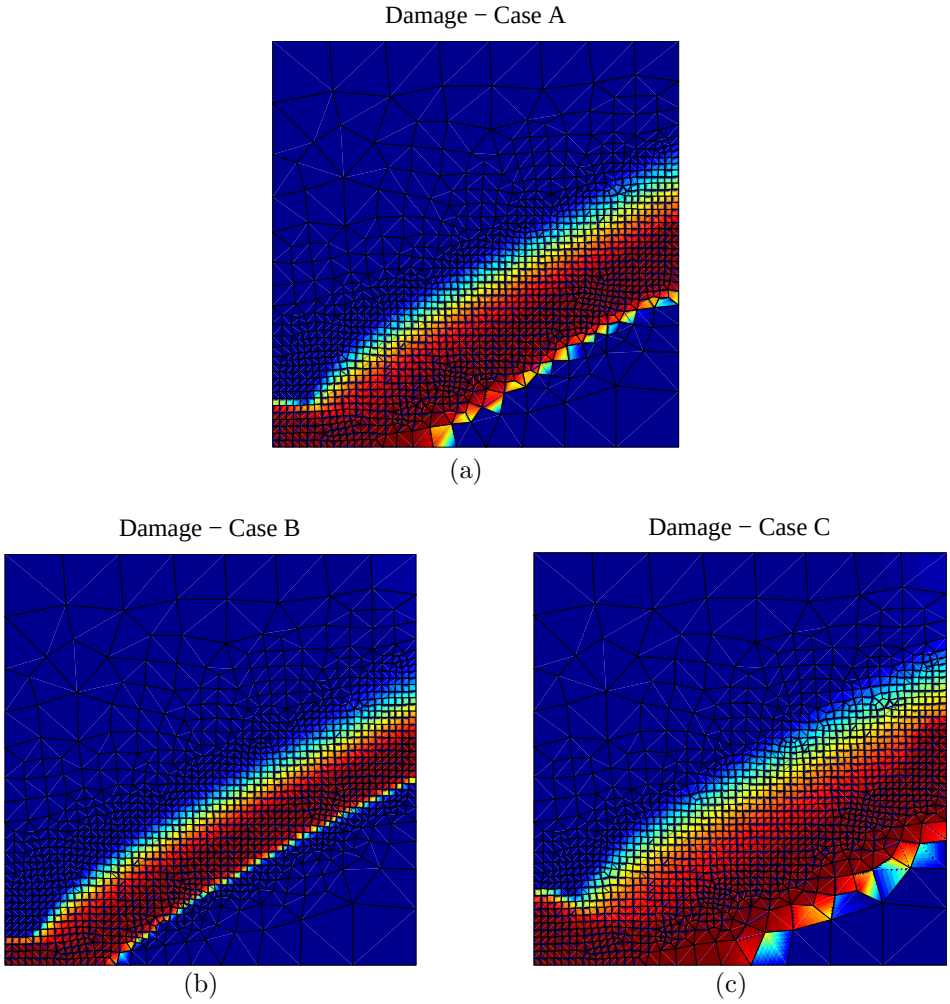

Figure 3.17: Shear test: damage field for cases A, B and C, with different characteristic lengths ℓ.

However, the damage fields of the three cases, plotted for the same load step, exhibit different widths. This is due to the action of diffusion, controlled by the characteristic length ℓ. As expected, the greater the characteristic length is, the wider damage field is exhibited.

The need for a gradual transient gradient activity

It has been shown that in order to obtain a realistic behaviour of a sharp crack, it is necessary to switch off diffusion once the specimen is divided into two parts. If a transient –rather than constant– diffusion is used, the physically unrealistic damage plateau is avoided. In this case, a binary transient gradient activity is used, controlled by means of the function $g(d)$ defined in Eq. (3.13) and depicted in Figure 3.7. However, from

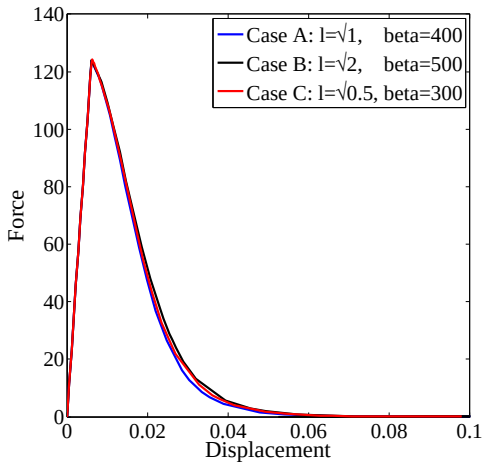

Figure 3.18: Shear test: force-displacement response for different materials.

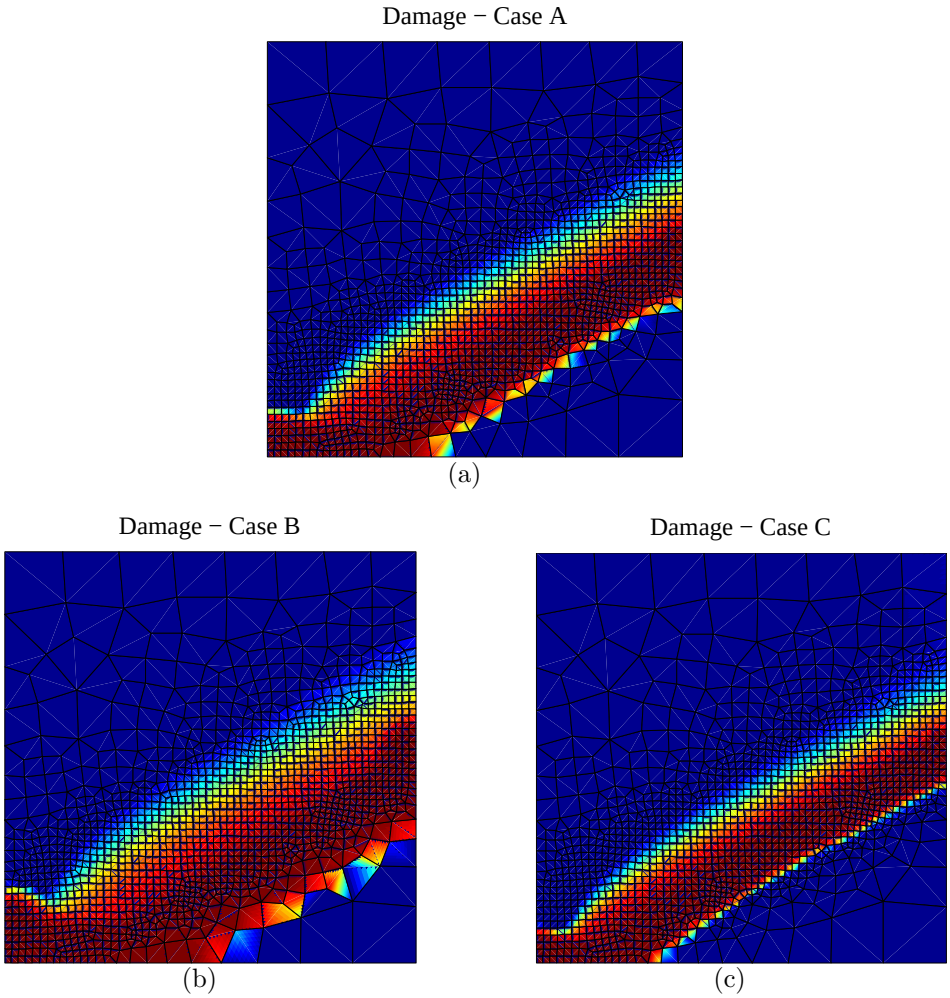

Figure 3.19: Shear test: damage field for cases A, B and C, with different materials, parameters ℓ and β.

this figure it can be observed that the function is not differentiable when $d = 1$. As a consequence, convergence is difficult to attain, requiring too lax tolerances in Newton's iterations.

The consequences of these lax tolerances can be noted if, once the specimen is divided into two parts, the prescribed displacements are still applied. As already discussed, the damage profile should no longer evolve. For case A (Table 3.2), the damage field is plotted for the states defined in Figure 3.20. It can be observed in Figure 3.21 how damage continues spreading even if the shear band is fully degraded, $d = 1$.

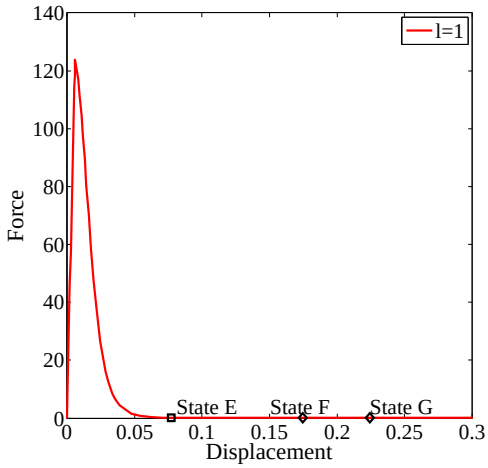

Figure 3.20: Shear test: force-displacement response.

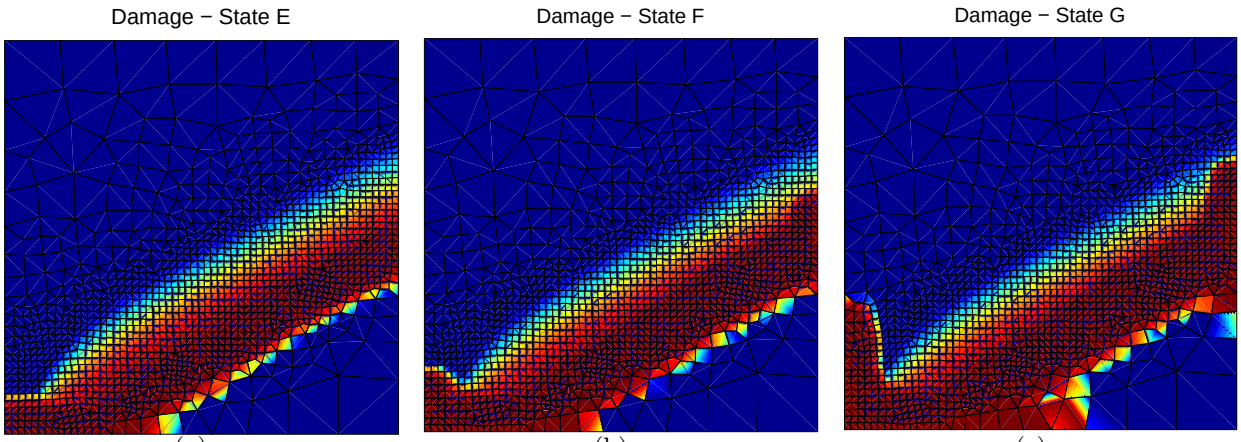

Figure 3.21: Shear test: damage field for states E, F and G.

With the purpose of avoiding these convergence problems, a gradual –rather than binary– gradient activity control function $g(d)$, differentiable in all the domain, is presented in Chapter 4.

Chapter 4

Continuous damage model with gradual gradient activity

The aim of this chapter is to present a damage model with gradual transient activity that can avoid the non-local interaction once the material is fully degraded.

In the previous chapter, the binary gradient control function $g(d)$ used produced convergence problems. In this case, an alternative definition of the function is discussed

$$g(d) = 1 - d^p \tag{4.1}$$

where p is a shape parameter.

With this definition, diffusion decreases as damage grows, becoming zero once damage reaches its maximum value, $d = 1$. In Figure 4.1, it can be noted that this function is differentiable in all the domain $d \in [0, 1]$.

The shape parameter p controls the smoothness of the function. For $p > 1$, it can be observed that the higher the parameter is, the steeper is the slope when d is close to 1. For $p < 1$, the slope has a value of $-\infty$ when $d = 0$, so the computation cannot be carried out.

The objective of this analysis is to work with a gradient activity similar to the binary one presented in Chapter 3. This means that diffusion is active until the specimen is fully damaged, when diffusion is switched off. Therefore, the interest is focused on values of $p > 1$, as great as possible.

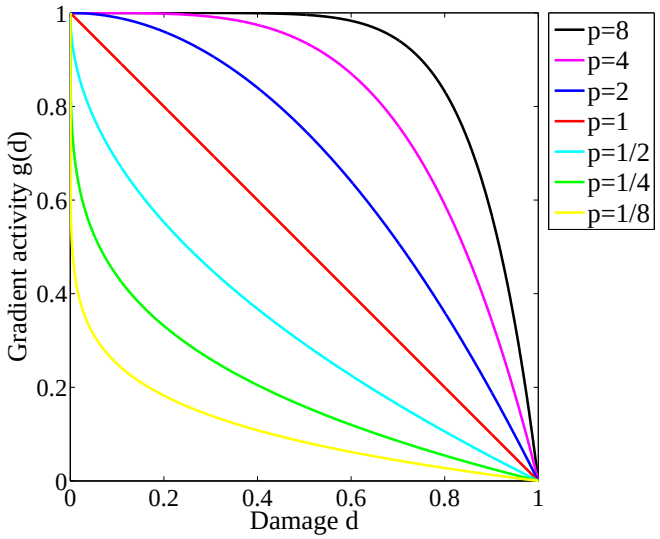

Figure 4.1: Gradient activity control function for different shape parameters.

Due to the definition of the gradient activity control function, some changes need to be made to the original variational formulation and following problem linearisation. As discussed in Eq. (3.5), (3.6) and (3.7), the damage parameter d depends on the non-local strains $\widetilde{\boldsymbol{\varepsilon}}$, and therefore, on the non-local displacements $\widetilde{\mathbf{u}}$. Considering that g is a function of d, it also depends on $\widetilde{\mathbf{u}}$.

In the following sections, the variational formulation and consistent linearisation of the gradual gradient activity problem are developed. In Section 4.1, a one-dimensional particularisation of the uniaxial tension test is carried out. Finally in Section 4.2, the formulation is extended to the two-dimensional problem and validated with a two-dimensional uniaxial test.

4.1 One-dimensional particularisation

4.1.1 Variational formulation and discretisation

In this section, the regularisation equation for the one-dimensional problem is solved. Considering the definition of $g(\widetilde{u})$, the regularisation equation now reads

$$\widetilde{u} - \frac{\mathrm{d}}{\mathrm{d}x}\left[\ell^2 g(\widetilde{u})\frac{\mathrm{d}\widetilde{u}}{\mathrm{d}x}\right] = u \tag{4.2}$$

Following the weighted residuals method and considering the test function $v(x)$ such that $v(x) = 0$ on the Dirichlet boundary, the regularisation equation is cast in a weak form. Then, following standard procedures and applying the boundary conditions (3.2), see Appendix B for details, the variational statement reads

$$\int_0^L \widetilde{v} \cdot \widetilde{u}\,\mathrm{d}x + \ell^2 \int_0^L \frac{\mathrm{d}\widetilde{v}}{\mathrm{d}x} \cdot g(\widetilde{u}) \frac{\mathrm{d}\widetilde{u}}{\mathrm{d}x} \mathrm{d}x = \int_0^L \widetilde{v} \cdot u\,\mathrm{d}x \tag{4.3}$$

Regarding the finite element discretisation, local, non-local and virtual displacements read, respectively,

$$u(x) = \sum_{j=1}^{n} u_j N_j(x) \tag{4.4a}$$

$$\widetilde{u}(x) = \sum_{j=1}^{n} \widetilde{u}_j N_j(x) \tag{4.4b}$$

$$\widetilde{v}(x) = N_i(x) \tag{4.4c}$$

where N_i and N_j are the matrices of standard finite element shape functions.

Then, the discrete format of the regularisation equation (4.3), see Appendix C for details, leads to the discrete weak form

$$\mathbf{M}\widetilde{\mathbf{u}} + \ell^2 \mathbf{D}\widetilde{\mathbf{u}} = \mathbf{M}\mathbf{u} \tag{4.5}$$

where

$$M_{ij} = \int_0^L N_i N_j \mathrm{d}x \tag{4.6a}$$

$$D_{ij} = \int_0^L \frac{\mathrm{d}N_i}{\mathrm{d}x} g(\widetilde{u}) \frac{\mathrm{d}N_j}{\mathrm{d}x} \mathrm{d}x \tag{4.6b}$$

The linearisation of the equilibrium equation, see Rodríguez-Ferran et al. (2005), and the regularisation equation (4.5) results in the tangent matrix

$$\mathbf{K}_{\mathrm{tan}} = \begin{bmatrix} \mathbf{K}_{\mathbf{uu}} & \mathbf{K}_{\mathbf{u}\widetilde{\mathbf{u}}} \\ \mathbf{K}_{\widetilde{\mathbf{u}}\mathbf{u}} & \mathbf{K}_{\widetilde{\mathbf{u}}\widetilde{\mathbf{u}}} \end{bmatrix} \tag{4.7}$$

Particularly, the new contribution in the regularisation equation modifies the terms $\mathbf{K}_{\widetilde{\mathbf{u}}\mathbf{u}}$ and $\mathbf{K}_{\widetilde{\mathbf{u}}\widetilde{\mathbf{u}}}$, since they are defined as

$$\mathbf{K}_{\widetilde{\mathbf{u}},\mathbf{u}} = \frac{\partial \mathbf{r}_{\mathrm{regu}}}{\partial \mathbf{u}} = -\mathbf{M} \tag{4.8}$$

$$\mathbf{K}_{\widetilde{\mathbf{u}},\widetilde{\mathbf{u}}} = \frac{\partial \mathbf{r}_{\mathrm{regu}}}{\partial \widetilde{\mathbf{u}}} = \mathbf{M} + \ell^2 \mathbf{D} + \ell^2 \frac{\partial \mathbf{D}}{\partial \widetilde{\mathbf{u}}} \cdot \widetilde{\mathbf{u}} \tag{4.9}$$

where

$$\frac{\partial D_{ij}}{\partial \widetilde{u}} = \int_0^L \frac{\mathrm{d}N_i}{\mathrm{d}x} \frac{\mathrm{d}g}{\mathrm{d}\widetilde{u}} \frac{\mathrm{d}N_j}{\mathrm{d}x} \mathrm{d}x \tag{4.10}$$

with

$$\frac{\mathrm{d}g}{\mathrm{d}\widetilde{u}} = -p \cdot d^{p-1} \frac{\partial d}{\partial \kappa} \frac{\partial \kappa}{\partial \widetilde{\varepsilon}} \frac{\partial \widetilde{\varepsilon}}{\partial \widetilde{u}} \tag{4.11}$$

4.1.2 Uniaxial tension test

The uniaxial tension test analysed in Chapter 3 is used to explore the capabilities of the proposed formulation. The same geometrical and material parameters are used, as well as linear softening as damage evolution law, see Table 3.1.

The problem is discretised with a mesh of 100 one-dimensional finite elements. Regarding regularisation, the test is run for a characteristic length of $\ell = 1$. In order to introduce an artificial residual stiffness as defined in Eq. (3.2) and avoid singularity, a value of $q = 5$ is used. Therefore,

$$k_{\text{art}} = \max\left(10^{-5}, (1-d)\right). \tag{4.12}$$

Both the mechanical and the regularisation boundary conditions are prescribed using the Lagrange multipliers method, see Appendix A for details. Displacement control is used to compute the response of the material, which means that any snap-back would not be captured.

Effect of the shape parameter p

First, the influence of the shape parameter p is discussed. The simulation is run for different values of p, maintaining constant the characteristic length $\ell = 1$, which represents diffusion. The results are also compared to the case with constant diffusion, where it is not switched off.

The force-response for the different cases is shown in Figure 4.2(a). As expected, the higher the value of p, the greater is the area under the curve, so the more ductility is exhibited. This is due to the fact that the greater p, the greater g. Note that function g multiplies the diffusion term of the regularisation equation. In Figure 4.2(b), the damage field is plotted for the same load step for the different cases. Again, a greater value for p produces a higher diffusion; thus, a wider damage distribution is exhibited. Finally, it is

important to remark that the case with constant diffusion –no switching off– is the one with the highest diffusion: widest area beneath the force-displacement curve and widest damage distribution.

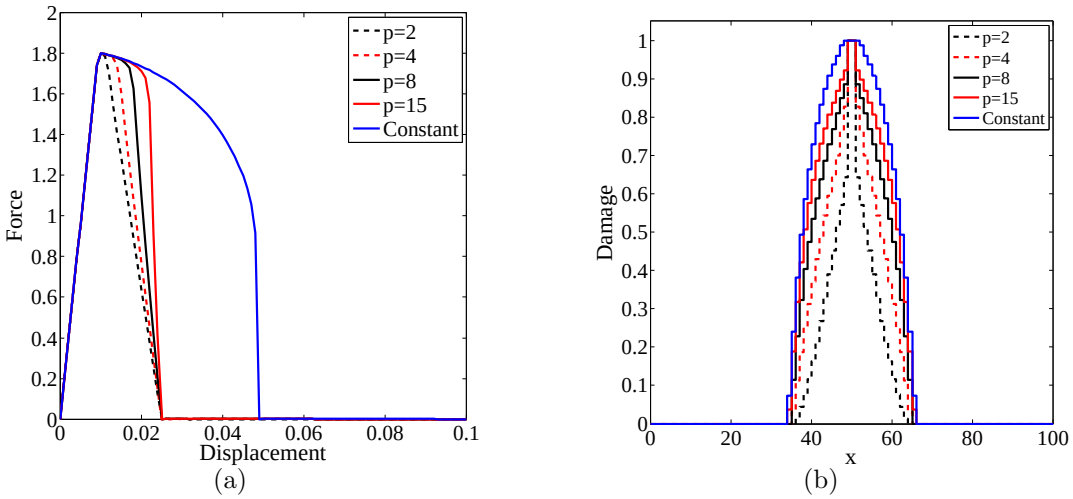

Figure 4.2: 1D-uniaxial test with gradual gradient activity: (a) force-displacement response and (b) damage profile for different values of p.

Regularisation capabilities

Regularisation (non-locality) is used in order to guarantee mesh independence of the damage band. The fact that diffusion has a value of zero (local model) once damage reaches its maximum value, may induce thinking that the regularisation capabilities of the model are lost. However, since the local model is only activated once $d = 1$ and not from the beginning, the results will still exhibit independence on the finite element size.

In this section, the same uniaxial tension test is simulated with different finite element sizes. In order to introduce an artificial residual stiffness as defined in Eq. (3.2) and avoid singularity, a value of $q = 5$ is used. Regarding regularisation, the test is run for a characteristic length of $\ell = 1$ and a shape parameter $p = 4$, see Eq. (3.3).

It can be observed in Figure 4.3, that the same damage distribution is obtained for different finite-element sizes of the bar. Therefore, it can be stated that gradual gradient activity successfully provides results which are independent on the finite-element mesh.

Effect of the characteristic length ℓ

Finally, this uniaxial tension test is carried out for two values of ℓ: $\ell = 1$ and $\ell = 2$. A

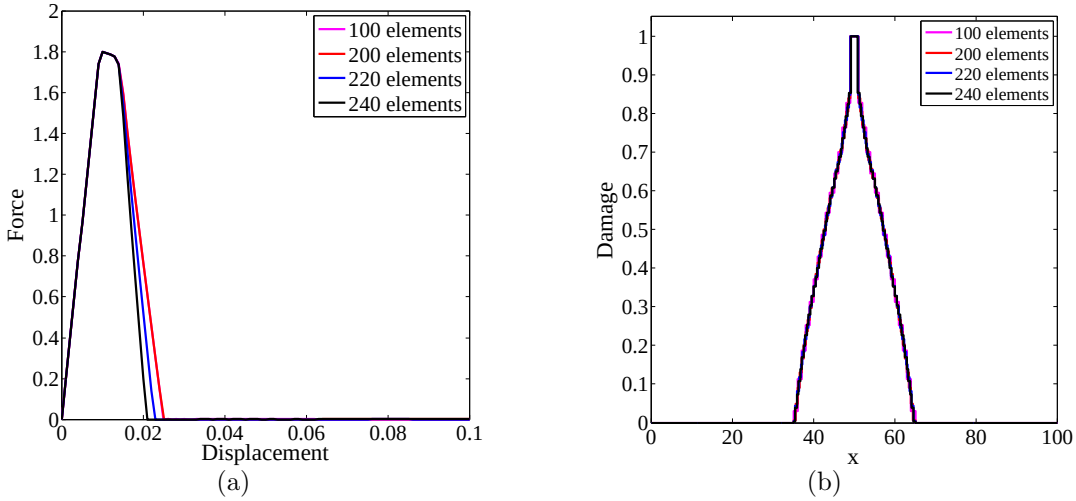

Figure 4.3: Uniaxial test with gradual gradient activity: (a) force-displacement response and (b) damage profile for different number of elements.

shape parameter of $p = 8$ is used in order to work with a gradient activity similar to the binary one. In order to introduce an artificial residual stiffness as defined in Eq. (3.2) and avoid singularity, a value of $q = 5$ is used.

The force-displacement response for the two cases is shown in Figure 4.4. As expected, the material with a higher characteristic length ℓ, exhibits a greater ductility.

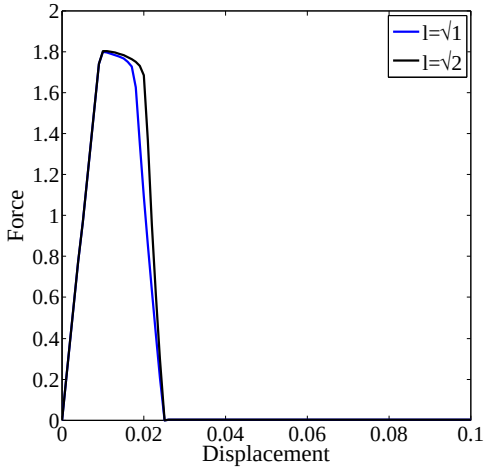

Figure 4.4: 1D-uniaxial test with gradual gradient activity: force-displacement response for different values of characteristic length ℓ.

In Figures 4.5 and 4.6, the damage, strains and displacement fields are exhibited for the case with $\ell = 1$ and $\ell = \sqrt{2}$, respectively. As expected, in the case with higher

characteristic length, both the damage and strains profiles are wider and the transition from the displacement field of the weakened part to the original one is smoother.

In both cases, the spurious load-carrying capacity is successfully avoided, since the forces reach zero once damage is maximum. Moreover, it can be observed that the damage distribution is the same for states E and F, i.e., no unrealistic damage plateau of value $d = 1$ is exhibited.

Finally, it is also important to remark that once damage reaches its maximum value $d = 1$ (states E and F), as the gradient activity control function is $g = 0$, diffusion is switched off. Thus, the damage model becomes local. This can be effectively observed in the strains field $\big($Figures 4.5(d) and 4.6(d)$\big)$, where for the mentioned states, strains are localised in the central –fully degraded– element.

Therefore, it can be stated that the damage model with gradual gradient activity is suitable for representing sharp cracks in one-dimensional problems: both a zero load-carrying capacity and a zero non-local interaction are obtained when the specimen is divided into two fully independent parts.

4.2 Two-dimensional extension

4.2.1 Variational formulation and discretisation

In this section, the regularisation equation for the two-dimensional problem is solved. This equation now reads

$$\widetilde{\mathbf{u}} - \nabla \cdot \big(\ell^2 g(\widetilde{\mathbf{u}}) \nabla \widetilde{\mathbf{u}}\big) = \mathbf{u} \tag{4.13}$$

Following the weighted residuals method and considering the test function $\widetilde{\mathbf{v}}(\mathbf{x})$ such that $\widetilde{\mathbf{v}}(\mathbf{x}) = \mathbf{0}$ on the Dirichlet boundary, the regularisation equation is cast in a weak form. Then, following standard procedures and applying the boundary conditions (3.2), see Appendix B for details, the variational statement reads

$$\int_\Omega \widetilde{\mathbf{v}} \cdot \widetilde{\mathbf{u}} \, \mathrm{d}\Omega + \ell^2 \int_\Omega g \, \nabla \widetilde{\mathbf{v}} : \nabla \widetilde{\mathbf{u}} \, \mathrm{d}\Omega = \int_\Omega \widetilde{\mathbf{v}} \cdot \mathbf{u} \, \mathrm{d}\Omega + \ell^2 \int_{\partial\Omega} g \, (\widetilde{\mathbf{v}} \cdot \mathbf{t}) \, (\mathbf{n} \cdot \nabla \mathbf{u} \cdot \mathbf{t}) \, \mathrm{d}\Gamma \tag{4.14}$$

The local, non-local and virtual displacement fields are discretised using two-dimensional shape functions as in Equations (4.4). Then, the discrete format of the regularisation

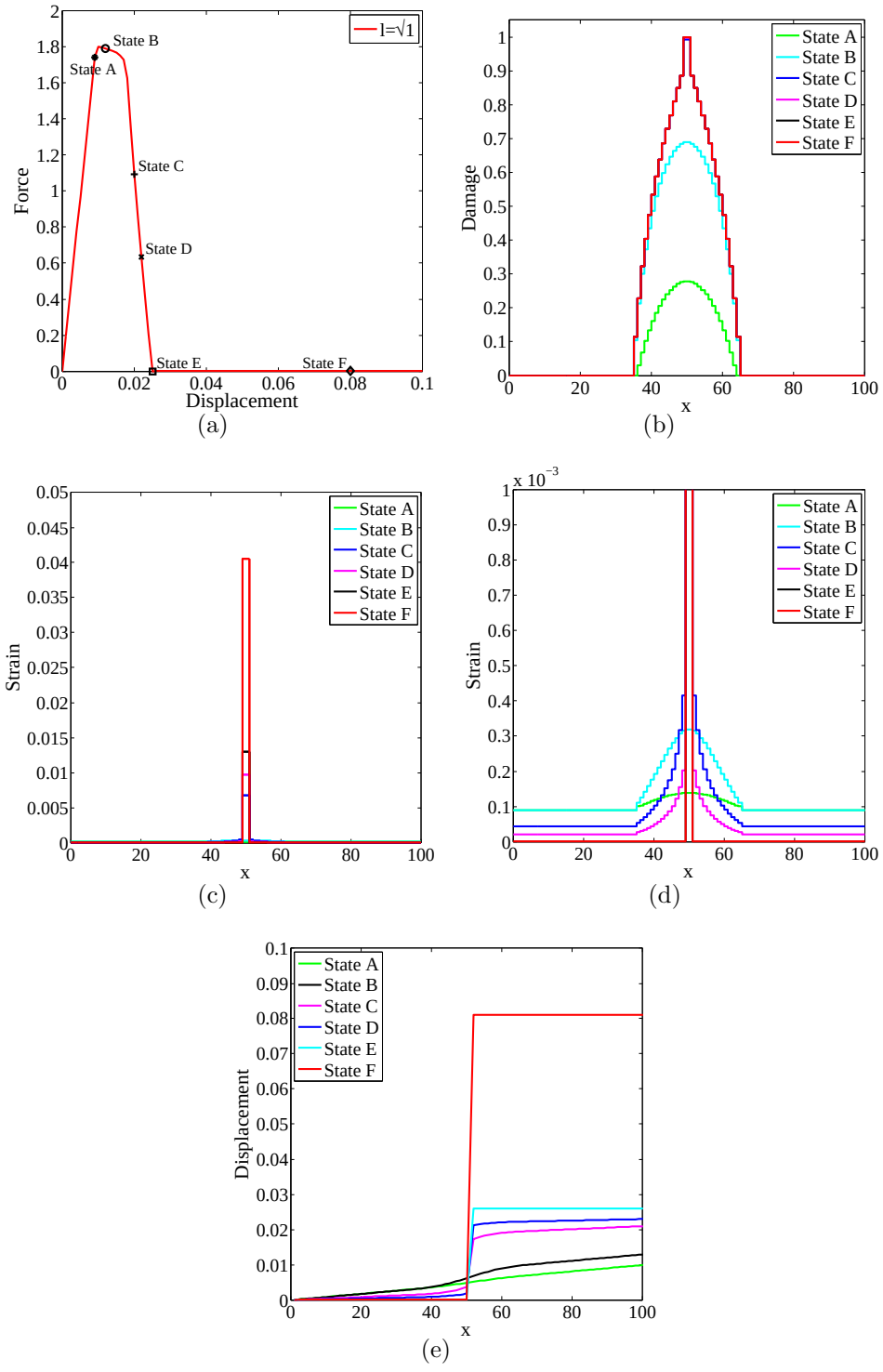

Figure 4.5: Results for the 1D-uniaxial test ($\ell = 1$) with gradual gradient activity: (a) force-displacement response, (b) damage distribution, (c) and (d) strain distribution and (e) displacement profiles.

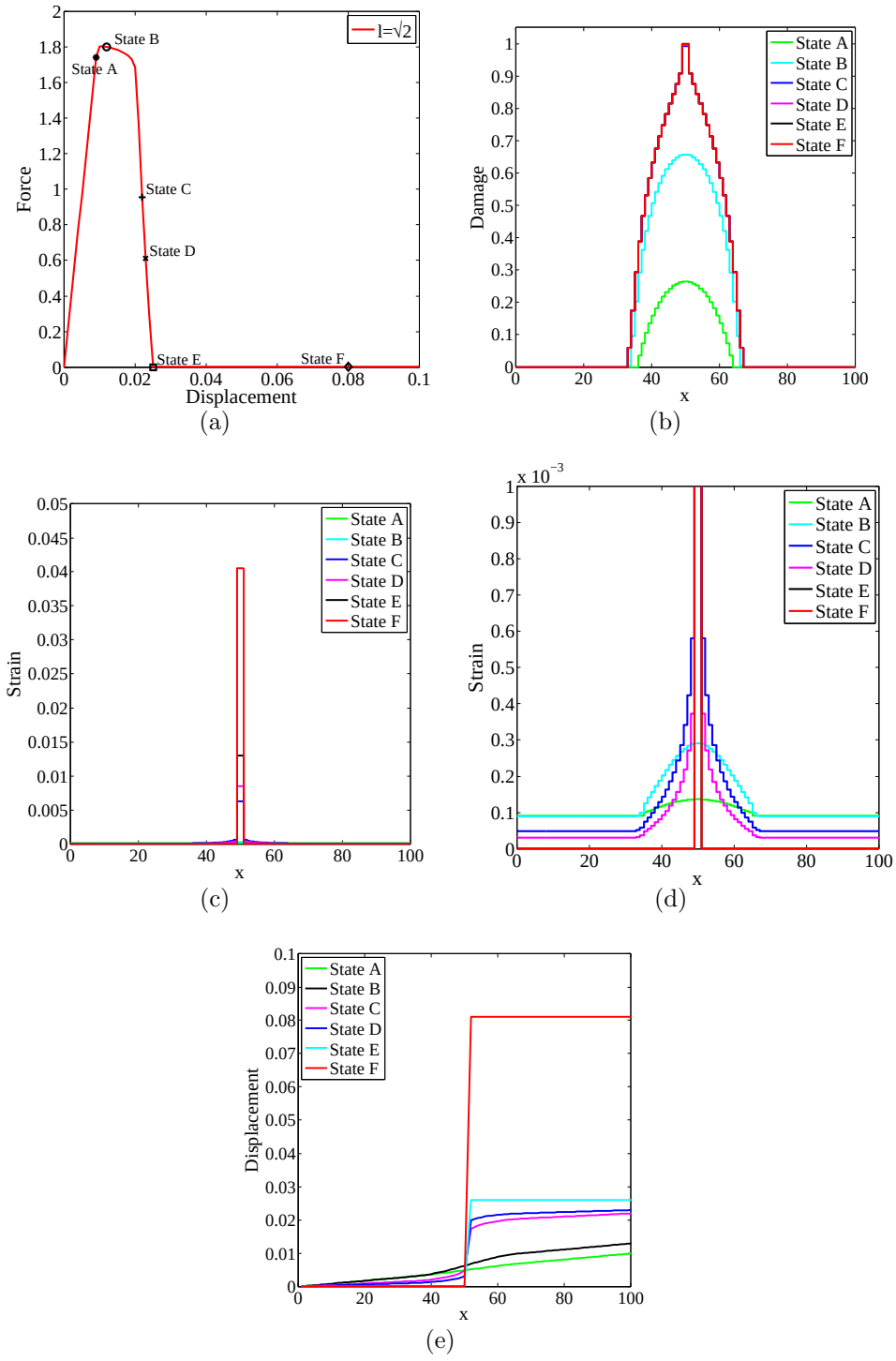

Figure 4.6: Results for the 1D-uniaxial test ($\ell = \sqrt{2}$) with gradual gradient activity: (a) force-displacement response, (b) damage distribution, (c) and (d) strain distribution and (e) displacement profiles.

equation (4.14), leads to the discrete weak form

$$\mathbf{M}\widetilde{\mathbf{u}} + \ell^2\mathbf{D}\widetilde{\mathbf{u}} = \mathbf{M}\mathbf{u} + \ell^2\mathbf{K}_{\mathrm{BC}}\mathbf{u} \tag{4.15}$$

where

$$\mathbf{D} = \int_\Omega g\,\nabla\mathbf{N}^T\nabla\mathbf{N}\,\mathrm{d}\Omega \tag{4.16}$$

$$\mathbf{K}_{\mathrm{BC}} = \int_{\partial\Omega} g\,\mathbf{N}^{\mathrm{T}}\mathbf{t}^{\mathrm{T}}\mathbf{t}\mathbf{n}^{\mathrm{T}}\nabla\mathbf{N}\,\mathrm{d}\Gamma \tag{4.17}$$

In this case, the terms $\mathbf{K}_{\widetilde{\mathbf{u}}\mathbf{u}}$ and $\mathbf{K}_{\widetilde{\mathbf{u}}\widetilde{\mathbf{u}}}$ of the tangent matrix (4.7) are defined as

$$\mathbf{K}_{\widetilde{\mathbf{u}},\mathbf{u}} = \frac{\partial\mathbf{r}_{\mathrm{regu}}}{\partial\mathbf{u}} = -(\mathbf{M} + \ell^2\mathbf{K}_{\mathrm{BC}}) \tag{4.18}$$

$$\mathbf{K}_{\widetilde{\mathbf{u}},\widetilde{\mathbf{u}}} = \frac{\partial\mathbf{r}_{\mathrm{regu}}}{\partial\widetilde{\mathbf{u}}} = \mathbf{M} + \ell^2\mathbf{D} + \ell^2\frac{\partial\mathbf{D}}{\partial\widetilde{\mathbf{u}}}\cdot\widetilde{\mathbf{u}} - \ell^2\frac{\partial\mathbf{K}_{\mathrm{BC}}}{\partial\widetilde{\mathbf{u}}}\cdot\mathbf{u} \tag{4.19}$$

where

$$\frac{\partial\mathbf{D}}{\partial\widetilde{\mathbf{u}}} = \int_\Omega \frac{\partial g}{\partial\widetilde{\mathbf{u}}}\,\nabla\mathbf{N}^{\mathrm{T}}\nabla\mathbf{N}\,\mathrm{d}\Omega \tag{4.20}$$

$$\frac{\partial\mathbf{K}_{\mathrm{BC}}}{\partial\widetilde{\mathbf{u}}} = \int_{\partial\Omega} \frac{\partial g}{\partial\widetilde{\mathbf{u}}}\,\mathbf{N}^{\mathrm{T}}\mathbf{t}^{\mathrm{T}}\,\mathbf{t}\,\mathbf{n}^{\mathrm{T}}\nabla\mathbf{N}\,\mathrm{d}\Gamma \tag{4.21}$$

4.2.2 Uniaxial tension test

The uniaxial tension test analysed in previous sections is simulated once more to explore the capabilities of the proposed two-dimensional formulation. The same geometrical and material parameters are used, see Table 3.1, and discretisation is carried out with a mesh of 100×1 two-dimensional quadrilateral finite elements. The influence of the main features of the gradual gradient activity formulation, the shape parameter p and the characteristic length ℓ, are also examined.

Effect of the shape parameter p

The objective of this formulation is to work with a gradual transient diffusion as similar as possible to the binary case, where diffusion is active and constant during all the damaging process until the moment where damage is maximum and the material is totally degraded, when it is switched off. In order to attain this behaviour with the gradual transient activity defined in Eq. (4.1), a high value of the shape parameter p should be considered. However, the higher the parameter, the more non-linear is the problem; hence, the more difficult it is to solve.

The simulation is run for a fixed value of characteristic length $\ell = 1$ and for different values of shape parameter p. In order to introduce an artificial stiffness as defined in Eq. (3.2), a value of $q = 5$ is used.

The force-displacement response and damage profiles obtained are shown in Figure 4.7. The damage distribution plotted corresponds to the damage state when the displacement of the free end of the bar is $u_{bar} = 0.05$. Results for different values of p are also compared with the constant case, where diffusion is not switched off. As expected, the higher the shape parameter p is, the more ductile material is obtained. Indeed, the higher p, the more similar to the constant case the force-displacement curve is. Moreover, a wider damage distribution is exhibited as the shape parameter p increases.

However, note how for the higher values $p = 20, p = 50$ and $p = 100$, the damage profile is not physically realistic since the entire bar has a value of $d = 1$. In fact, it can be observed that the force-displacement curves for these values exhibit a large force jump just before reaching a value of zero force. This sudden drop in force is caused by the displacement control strategy. With an appropriate arc-length control, a snap-back response with physically realistic damage profile would be obtained.

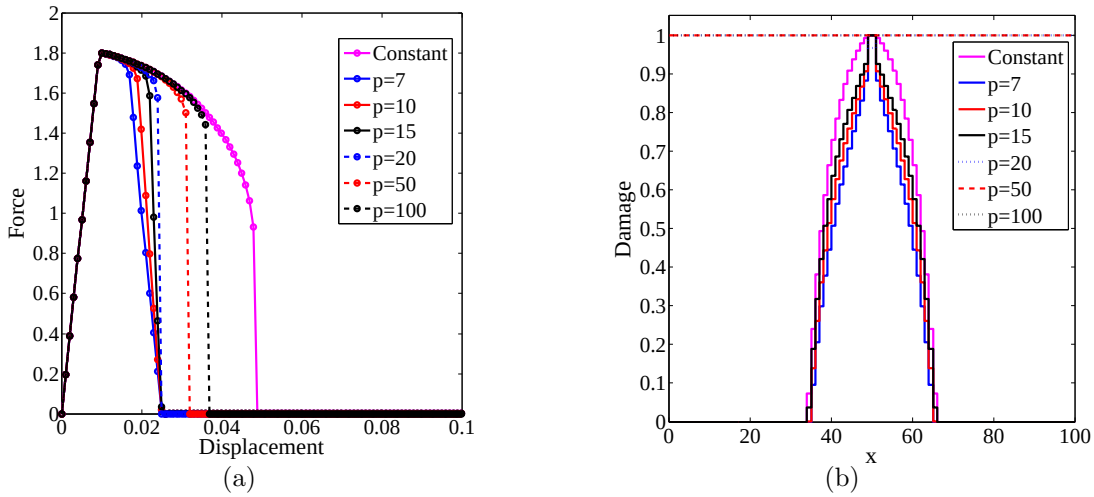

Figure 4.7: 2D-uniaxial test with gradual gradient activity: (a) force-displacement response and (b) damage profile for different values of p.

Therefore, it can be stated that a high value of the shape parameter p effectively provides a material behaviour more resembling to the binary case. However, too high values increase the non-linearity of the problem, and thus, its difficulty to be solved. This can lead to both impossibility to attain convergence or unrealistic results.

Effect of the characteristic length ℓ

As already mentioned, the characteristic length ℓ corresponds to a diffusion parameter in the regularisation PDE (4.13). Generally, a high value of diffusion is conceived to help smoothing the problem and thus, improve the efficiency of the solving process. However, since the model is based on a transient gradient activity where diffusion is switched off, the higher the parameter, the higher the difference with the switched off value $\ell = 0$. If the difference between the original parameter and $\ell = 0$ is too high, convergence problems may occur.

In this case, the simulation is run for a fixed value of the shape parameter $p = 8$ and for different values of the characteristic length ℓ. In order to introduce an artificial stiffness as defined in Eq. (3.2), a value of $q = 5$ is used.

The results obtained are shown in Figure 4.8. The damage distribution plotted corresponds to the damage state when the displacement of the free end of the bar is $u_{bar} = 0.05$. As expected, higher values of characteristic length provide more ductile force-displacement responses and wider damage distributions. However, it can be observed that for too high values, $\ell = \sqrt{2}, \ell = \sqrt{10}$ and $\ell = \sqrt{20}$, the damage distribution is not physically realistic, having the entire or most of the bar a maximum value of damage, $d = 1$. This is due to the fact that the difference between the original value and $\ell = 0$ is to large, fact that causes convergence problems or inaccurate results.

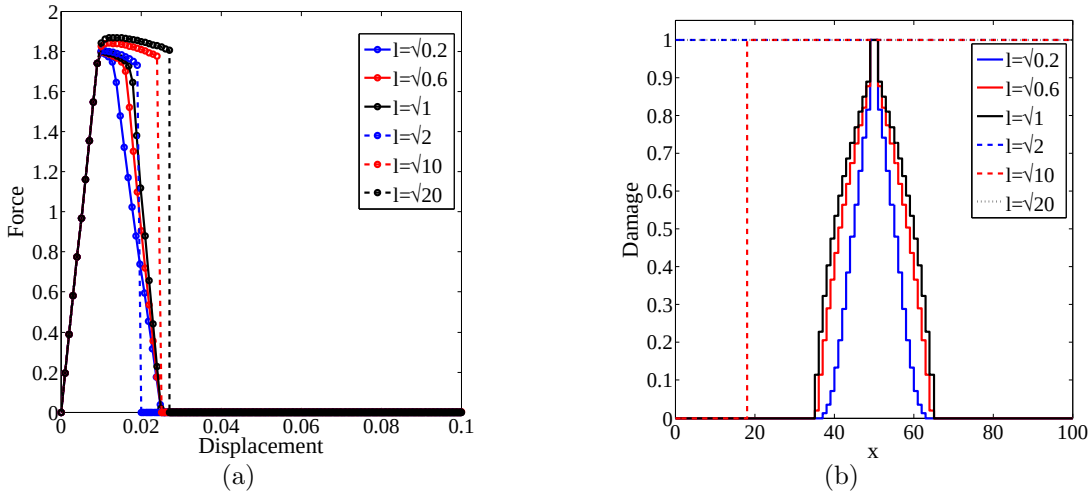

Figure 4.8: 2D-uniaxial test with gradual gradient activity: (a) force-displacement response and (b) damage profile for different values of ℓ.

Finally, the test is discussed for a shape parameter $p = 8$ and a characteristic length of $\ell = 1$, which are values that have performed successfully on the simulations.

Figure 4.9 shows the results obtained. In the force-displacement response it can be seen that the spurious load-carrying capacity has been successfully avoided, being the forces able to reach a value of zero. Besides, no unrealistic damage plateau of value $d = 1$ is observed, so any non-local interaction has not been exhibited. Again, the strains are localised in one element once the material is fully damaged (Figure 4.9(c), which corresponds to the switching off diffusion once $d = 1$. Finally, it can be noted that the results coincide with the one-dimensional case, which supports the validation of the model.

After these simulations, it can be stated that the proposed adjustments for non-local damage models regarding gradual gradient activity are suitable for effectively representing a sharp discontinuity in a continuous setting.

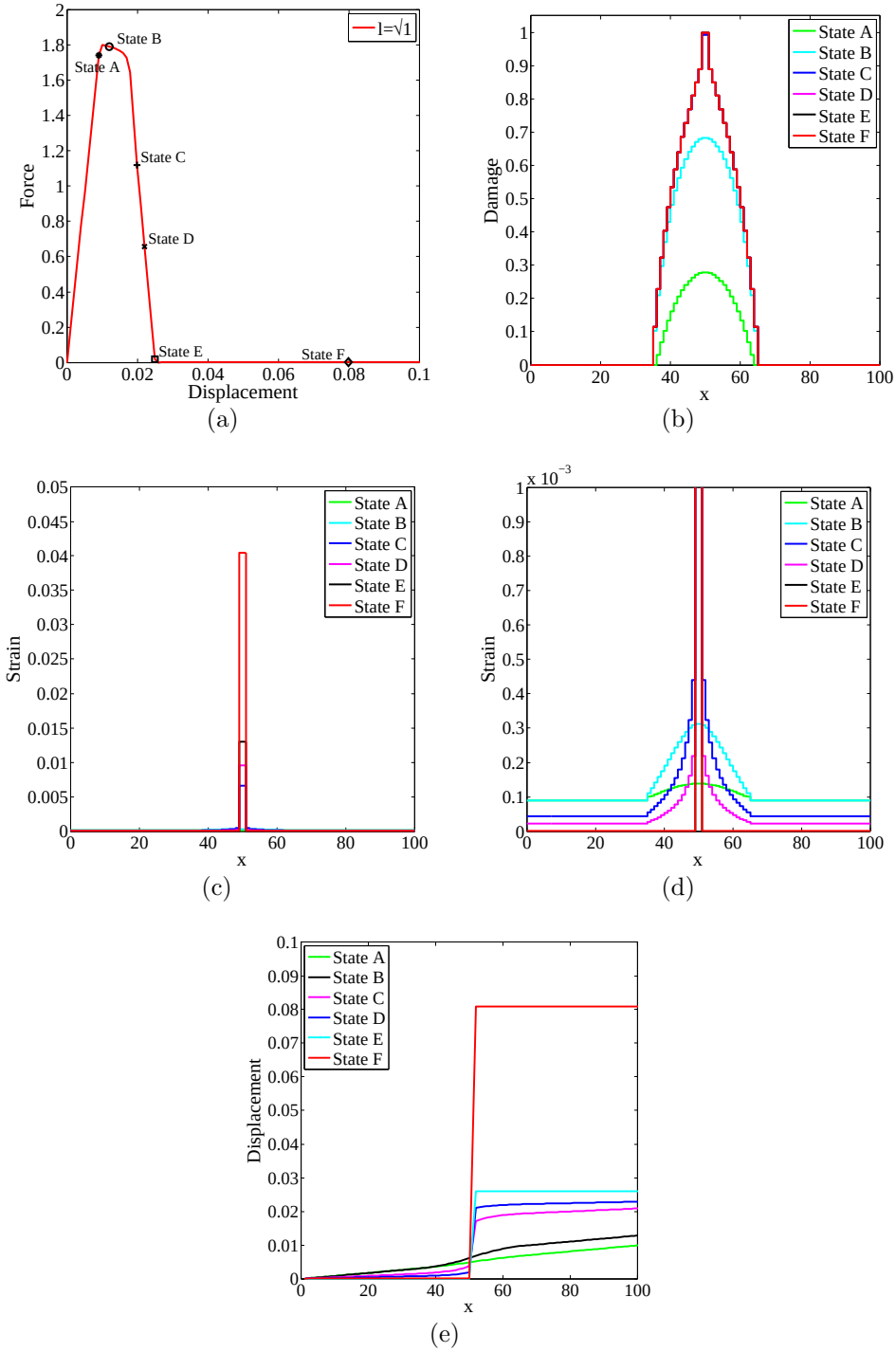

Figure 4.9: Results for the 2D-uniaxial test ($\ell = 1$) with gradual gradient activity: (a) force-displacement response, (b) damage distribution, (c) and (d) strain distribution and (e) displacement profiles.

Chapter 5

Concluding remarks and future work

5.1 Concluding remarks

In this dissertation a finite element approach to mimic a sharp discontinuity within a continuous setting has been developed. To this end, two main contributions discussed in detail in the previous chapters are presented:

1. **An adjustment that allows to have zero load-carrying capacity has been proposed.** A procedure where an artificial stiffness is applied without altering the constitutive equation is presented in Chapter 3. First, an alternative definition of the stiffness matrix that will not limit the value of the damage parameter has been discussed. Then, a numerical uniaxial tension test has been carried out to successfully validate this technique. Therefore, it can be stated that once the material is fully degraded, the proposed methodology provides a zero load-carrying capacity.

2. **An adjustment that allows to have zero non-local interaction has been proposed.** In order to avoid the unrealistic damage plateau of value $d = 1$ once the specimen is fully degraded, provided by constant gradient activity, two new approaches have been proposed:

    1. **Binary gradient activity**. In Chapter 3, a new formulation of the damage model, based on binary transient diffusion has been presented. In this approach, the diffusion is set constant until the specimen is fully degraded, when

it is set to zero. However, the gradient control function is not differentiable in $d = 1$, which leads to convergence problems. The proposed model has been tested for some numerical simulations. For simple tests, the results obtained have been satisfactory and the regularisation capabilities have been verified. However, a complex shear band test yields inaccurate results and convergence problems due to the definition of the gradient control function.

2. **Gradual gradient activity**. With the aim of solving this convergence issue, in Chapter 4, a damage model based on gradual transient diffusion is presented. In this approach, diffusion gradually decreases as damage increases, reaching a value of zero when damage is maximum. In this case, the gradient control function is differentiable in all the domain. The capabilities of the proposed approach have been verified by performing both one- and two-dimensional simulations of a uniaxial tension test, which have provided accurate results and have also validated the regularisation capabilities of the transient gradient model.

Hence, the model provides a satisfactory replication of sharp cracks, defined by exhibiting a zero load-carrying capacity and zero non-local interaction.

5.2 Future work

The work carried out in this dissertation leaves several directions to be discussed in the near future. These open research lines can be summarised as

- **To validate the gradual model with two-dimensional examples.** The gradual gradient activity formulation proposed in this work has been validated with a one- and two-dimensional uniaxial tension test. In order to carry out a thorough validation of this approach, some other two-dimensional simulations could be run, such as the shear band test discussed in Section 3.4 or a four-point bending test.

- **To examine a new definition of the gradient activity control function g**. It has been determined that for too high shape parameters p, the slope of the gradient activity control function g is too steep and causes convergence difficulties. In order to obtain a more smooth function, a new definition could be analysed, for instance $g(d) = (1 - d)^p$, as proposed by Miehe et al. (2015).

- **To explore new applications of the proposed artificial stiffness formulation.** There exist other models, such as phase field approaches, that use a numerically motivated artificial stiffness that also affects the mechanical response of the material. It would be interesting to extend the proposed artificial stiffness formulation to other models and find an alternative way to avoid singularity of the secant stiffness matrix without altering the constitutive equation.

Appendix A

Lagrange multipliers

This appendix deals with the treatment of Dirichlet boundary conditions with Lagrange multipliers, see Belytschko et al. (2000). Special attention is given to the treatment of the mechanical and the regularisation boundary conditions. The formulation is developed for the two-dimensional problem.

On the one hand, finite element discretisation of the weak form of the equilibrium and regularisation equations leads to the two discrete weak forms

$$\mathbf{r}_{\text{equil}}(\mathbf{u}, \widetilde{\mathbf{u}}) := \mathbf{f}_{\text{int}}(\mathbf{u}, \widetilde{\mathbf{u}}) - \mathbf{f}_{\text{ext}} = \mathbf{0} \tag{A.0.1a}$$

$$\mathbf{r}_{\text{regu}}(\mathbf{u}, \widetilde{\mathbf{u}}) := -(\mathbf{M} + \ell^2 \mathbf{K}_{\text{BC}})\mathbf{u} + (\mathbf{M} + \ell^2 \mathbf{D})\widetilde{\mathbf{u}} = \mathbf{0} \tag{A.0.1b}$$

On the other hand, the Dirichlet boundary conditions for the mechanical and the regularisation problem, respectively, are defined as

$$\mathbf{A}_{\text{equil}}\mathbf{u} = \mathbf{u}^* \tag{A.0.2a}$$

$$\mathbf{A}_{\text{regu}}\mathbf{u} = \mathbf{A}_{\text{regu}}\widetilde{\mathbf{u}} \quad \Rightarrow \quad \mathbf{A}_{\text{regu}}(\mathbf{u} - \widetilde{\mathbf{u}}) = \mathbf{0} \tag{A.0.2b}$$

Then, the global system can be summarised as

$$\begin{bmatrix} \mathbf{K}_{\mathbf{u},\mathbf{u}} & \mathbf{K}_{\mathbf{u},\tilde{\mathbf{u}}} & | & \mathbf{A}_{\text{equil}}^{\text{T}} & \mathbf{0} \\ \mathbf{K}_{\tilde{\mathbf{u}},\mathbf{u}} & \mathbf{K}_{\tilde{\mathbf{u}},\tilde{\mathbf{u}}} & | & \mathbf{0} & \mathbf{A}_{\text{regu}}^{\text{T}} \\ — & — & — & — & — \\ \mathbf{A}_{\text{equil}} & \mathbf{0} & | & \mathbf{0} & \mathbf{0} \\ \mathbf{A}_{\text{regu}} & -\mathbf{A}_{\text{regu}} & | & \mathbf{0} & \mathbf{0} \end{bmatrix} \begin{bmatrix} \delta\mathbf{u} \\ \delta\tilde{\mathbf{u}} \\ \\ \delta\boldsymbol{\lambda}_{\text{equil}} \\ \delta\boldsymbol{\lambda}_{\text{regu}} \end{bmatrix} = \begin{bmatrix} -\mathbf{r}_{\text{equil}} \\ -\mathbf{r}_{\text{regu}} \\ \\ \mathbf{0} \\ \mathbf{0} \end{bmatrix} \tag{A.0.3}$$

where $\mathbf{A}_{\text{equil}}$ is the matrix of mechanical constraints, $\mathbf{A}_{\text{regu}}$ the matrix of regularisation constraints and

$$\mathbf{K}_{\mathbf{u},\mathbf{u}} = \frac{\partial \mathbf{r}_{\text{equil}}}{\partial \mathbf{u}} \tag{A.0.4a}$$

$$\mathbf{K}_{\mathbf{u},\tilde{\mathbf{u}}} = \frac{\partial \mathbf{r}_{\text{equil}}}{\partial \tilde{\mathbf{u}}} \tag{A.0.4b}$$

$$\mathbf{K}_{\tilde{\mathbf{u}},\mathbf{u}} = \frac{\partial \mathbf{r}_{\text{regu}}}{\partial \mathbf{u}} \tag{A.0.4c}$$

$$\mathbf{K}_{\tilde{\mathbf{u}},\tilde{\mathbf{u}}} = \frac{\partial \mathbf{r}_{\text{regu}}}{\partial \tilde{\mathbf{u}}} \tag{A.0.4d}$$

Note that the global matrix is not symmetric. This is due to the fact that Dirichlet boundary conditions for the regularisation problem tie $\mathbf{u}$ and $\tilde{\mathbf{u}}$.

Appendix B

Variational formulation and discretisation

In this appendix the variational formulation of the proposed model is derived: the regularisation equation with combined boundary conditions is cast in a weak form. First, in Section B.1, the variational formulation is developed for the one dimensional problem. In Section B.2, the formulation is extended to a two-dimensional setting.

B.1 One-dimensional problem

The regularisation equations reads

$$\widetilde{u} - \frac{\mathrm{d}}{\mathrm{d}x}\left[\ell^2 g(\widetilde{u})\frac{\mathrm{d}\widetilde{u}}{\mathrm{d}x}\right] = u \tag{B.1.1}$$

where u and $\widetilde{u}$ are the local and non-local displacements, respectively, ℓ^2 the characteristic length and g the gradient activity control function.

By multiplying Eq. (B.1.1) by an arbitrary virtual displacement field $\widetilde{v}(x)$ (i.e. test function) such that $\widetilde{v}(x) = 0$ on the Dirichlet boundary and integrating over the domain

Ω, the regularisation equation is cast in a weak form

$$\int_0^L \widetilde{v} \cdot \widetilde{u} \, \mathrm{d}x - \ell^2 \int_0^L \widetilde{v} \cdot \frac{\mathrm{d}}{\mathrm{d}x} \left[g(\widetilde{u}) \frac{\mathrm{d}\widetilde{u}}{\mathrm{d}x} \right] \mathrm{d}x = \int_0^L \widetilde{v} \cdot u \, \mathrm{d}x \tag{B.1.2}$$

Using integration by parts it can be observed that the second integral in Eq. (B.1.2) can be expressed as

$$\int_0^L \widetilde{v} \cdot \frac{\mathrm{d}}{\mathrm{d}x} \left[g(\widetilde{u}) \frac{\mathrm{d}\widetilde{u}}{\mathrm{d}x} \right] \mathrm{d}x = \int_0^L \frac{\mathrm{d}}{\mathrm{d}x} \left[\widetilde{v} \cdot g(\widetilde{u}) \frac{\mathrm{d}\widetilde{u}}{\mathrm{d}x} \right] \mathrm{d}x - \int_0^L \frac{\mathrm{d}\widetilde{v}}{\mathrm{d}x} \cdot g(\widetilde{u}) \frac{\mathrm{d}\widetilde{u}}{\mathrm{d}x} \mathrm{d}x \tag{B.1.3}$$

Therefore, considering the boundary conditions defined in Eq. (3.2), the variational formulation can be derived

$$\int_0^L \widetilde{v} \cdot \widetilde{u} \, \mathrm{d}x + \ell^2 \int_0^L \frac{\mathrm{d}\widetilde{v}}{\mathrm{d}x} \cdot g(\widetilde{u}) \frac{\mathrm{d}\widetilde{u}}{\mathrm{d}x} \mathrm{d}x = \int_0^L \widetilde{v} \cdot u \, \mathrm{d}x \tag{B.1.4}$$

B.2 Two-dimensional problem

For the two-dimensional problem, the regularisation equation reads

$$\widetilde{\mathbf{u}} - \nabla \cdot \left(\ell^2 g(\widetilde{\mathbf{u}}) \nabla \widetilde{\mathbf{u}} \right) = \mathbf{u} \tag{B.2.1}$$

where $\mathbf{u}$ and $\widetilde{\mathbf{u}}$ are the local and non-local displacements, respectively, and ∇ the differential operator nabla.

The weighted residuals method is used to cast the regularisation equation (B.2.1) in a weak form. It is multiplied by an arbitrary virtual displacement field $\widetilde{\mathbf{v}}(\mathbf{x})$ such that $\widetilde{\mathbf{v}}(\mathbf{x}) = \mathbf{0}$ on the Dirichlet boundary and integrated over the domain Ω as

$$\int_\Omega \widetilde{\mathbf{v}} \cdot \widetilde{\mathbf{u}} \, \mathrm{d}\Omega - \ell^2 \int_\Omega \widetilde{\mathbf{v}} \cdot \nabla \cdot (g \, \nabla \widetilde{\mathbf{u}}) \, \mathrm{d}\Omega = \int_\Omega \widetilde{\mathbf{v}} \cdot \mathbf{u} \, \mathrm{d}\Omega \tag{B.2.2}$$

Integrating by parts and considering Gauss divergence theorem, the second integral in Eq. (B.2.2) can be expressed as

$$\int_\Omega \widetilde{\mathbf{v}} \cdot \nabla \cdot (g \, \nabla \widetilde{\mathbf{u}}) \, \mathrm{d}\Omega = \int_\Omega \nabla \cdot (\widetilde{\mathbf{v}} \cdot g \nabla \widetilde{\mathbf{u}}) \, \mathrm{d}\Omega - \int_\Omega \nabla \widetilde{\mathbf{v}} : g \nabla \widetilde{\mathbf{u}} \, \mathrm{d}\Omega \tag{B.2.3}$$

$$= \int_{\partial\Omega} g \, \widetilde{\mathbf{v}} \cdot (\mathbf{n} \cdot \nabla \widetilde{\mathbf{u}}) \, \mathrm{d}\Gamma - \int_\Omega g \, \nabla \widetilde{\mathbf{v}} : \nabla \widetilde{\mathbf{u}} \, \mathrm{d}\Omega \tag{B.2.4}$$

where $\mathbf{n}$ is the outward unit normal defined on the boundary $\Gamma = \partial\Omega$.

Thus, the weak form can be expressed as

$$\int_\Omega \widetilde{\mathbf{v}} \cdot \widetilde{\mathbf{u}} \, \mathrm{d}\Omega - \ell^2 \int_{\partial\Omega} g \, \widetilde{\mathbf{v}} \cdot (\mathbf{n} \cdot \nabla \widetilde{\mathbf{u}}) \, \mathrm{d}\Gamma + \ell^2 \int_\Omega g \, \nabla \widetilde{\mathbf{v}} : \nabla \widetilde{\mathbf{u}} \, \mathrm{d}\Omega = \int_\Omega \widetilde{\mathbf{v}} \cdot \mathbf{u} \, \mathrm{d}\Omega \tag{B.2.5}$$

Boundary conditions

First, considering the Dirichlet boundary conditions in Eq. (3.2), it can be stated that $\widetilde{\mathbf{v}} \cdot \mathbf{n} = 0$. Thus, the virtual displacement $\widetilde{\mathbf{v}}$ is decomposed in its normal and tangential components as

$$\widetilde{\mathbf{v}} = (\widetilde{\mathbf{v}} \cdot \mathbf{n})\widetilde{\mathbf{v}} + (\widetilde{\mathbf{v}} \cdot \mathbf{t})\mathbf{t} = (\widetilde{\mathbf{v}} \cdot \mathbf{t})\mathbf{t} \tag{B.2.6}$$

and the term $\mathbf{n} \cdot \nabla \widetilde{\mathbf{u}}$ as

$$\mathbf{n} \cdot \nabla \widetilde{\mathbf{u}} = (\mathbf{n} \cdot \nabla \widetilde{\mathbf{u}} \cdot \mathbf{n})\mathbf{n} + (\mathbf{n} \cdot \nabla \widetilde{\mathbf{u}} \cdot \mathbf{t})\mathbf{t} \tag{B.2.7}$$

These two terms can be substituted in Eq. (B.2.5). Also, noting that $\mathbf{t} \cdot \mathbf{n} = 0$ and $\mathbf{t} \cdot \mathbf{t} = 1$, the second integral now reads

$$\int_{\partial\Omega} g \, \widetilde{\mathbf{v}} \cdot (\mathbf{n} \cdot \nabla \widetilde{\mathbf{u}}) \, \mathrm{d}\Gamma = \int_{\partial\Omega} \Big(g \, (\widetilde{\mathbf{v}} \cdot \mathbf{t})(\mathbf{n} \cdot \nabla \widetilde{\mathbf{u}} \cdot \mathbf{n}) + g \, (\widetilde{\mathbf{v}} \cdot \mathbf{t})(\mathbf{n} \cdot \nabla \widetilde{\mathbf{u}} \cdot \mathbf{t}) \Big) \mathrm{d}\Gamma \tag{B.2.8}$$

$$= \int_{\partial\Omega} g \, (\widetilde{\mathbf{v}} \cdot \mathbf{t})(\mathbf{n} \cdot \nabla \widetilde{\mathbf{u}} \cdot \mathbf{t}) \, \mathrm{d}\Gamma \tag{B.2.9}$$

Second, using the Neumann boundary conditions in Eq. (3.2), Eq. (B.2.9) reads

$$\int_{\partial\Omega} g \, (\widetilde{\mathbf{v}} \cdot \mathbf{t})(\mathbf{n} \cdot \nabla \widetilde{\mathbf{u}} \cdot \mathbf{t}) \, \mathrm{d}\Gamma = \int_{\partial\Omega} g \, (\widetilde{\mathbf{v}} \cdot \mathbf{t})(\mathbf{n} \cdot \nabla \mathbf{u} \cdot \mathbf{t}) \, \mathrm{d}\Gamma \tag{B.2.10}$$

Finally, the variational statement is obtained as

$$\int_\Omega \widetilde{\mathbf{v}} \cdot \widetilde{\mathbf{u}} \, \mathrm{d}\Omega + \ell^2 \int_\Omega g \, \nabla \widetilde{\mathbf{v}} : \nabla \widetilde{\mathbf{u}} \, \mathrm{d}\Omega = \int_\Omega \widetilde{\mathbf{v}} \cdot \mathbf{u} \, \mathrm{d}\Omega + \ell^2 \int_{\partial\Omega} g \, (\widetilde{\mathbf{v}} \cdot \mathbf{t}) \, (\mathbf{n} \cdot \nabla \mathbf{u} \cdot \mathbf{t}) \, \mathrm{d}\Gamma \tag{B.2.11}$$

Appendix C

Consistent linearisation of the equilibrium and regularisation equations

In this appendix, the consistent linearisation of the problem is presented. In Section C.1, the consistent tangent matrix of the one-dimensional problem is reviewed. In Section C.2, the formulation is extended to the two-dimensional setting.

C.1 One-dimensional problem

The finite element discretisation of the weak form of the equilibrium, see Rodríguez-Ferran et al. (2005), and regularisation, Eq. (B.1), equations leads to the two discrete weak forms

$$\mathbf{r}_{\text{equil}}(\mathbf{u}, \widetilde{\mathbf{u}}) := \mathbf{f}_{\text{int}}(\mathbf{u}, \widetilde{\mathbf{u}}) - \mathbf{f}_{\text{ext}} = \mathbf{0} \tag{C.1.1a}$$

$$\mathbf{r}_{\text{regu}}(\mathbf{u}, \widetilde{\mathbf{u}}) := -\mathbf{M}\mathbf{u} + (\mathbf{M} + \ell^2\mathbf{D})\widetilde{\mathbf{u}} = \mathbf{0} \tag{C.1.1b}$$

where

$$\mathbf{f}_{\text{int}} = \int_0^L \mathbf{B}^{\mathrm{T}} \boldsymbol{\sigma} \mathrm{d}x \tag{C.1.2a}$$

$$\mathbf{M} = \int_0^L \mathbf{N}^{\mathrm{T}} \mathbf{N} \mathrm{d}x \tag{C.1.2b}$$

$$\mathbf{D} = \int_0^L \nabla \mathbf{N}^{\mathrm{T}} g(\widetilde{\mathbf{u}}) \nabla \mathbf{N} \mathrm{d}x \tag{C.1.2c}$$

with $\mathbf{N}$ the matrix of shape functions, $\nabla\mathbf{N}$ the matrix of shape function gradients and $\mathbf{B}$ the matrix of shape functions derivatives.

Linearisation of Equations (C.1.1) results in the tangent matrix

$$\mathbf{K}_{\text{tan}} = \begin{bmatrix} \mathbf{K}_{\mathbf{uu}} & \mathbf{K}_{\mathbf{u}\widetilde{\mathbf{u}}} \\ \mathbf{K}_{\widetilde{\mathbf{u}}\mathbf{u}} & \mathbf{K}_{\widetilde{\mathbf{u}}\widetilde{\mathbf{u}}} \end{bmatrix} \tag{C.1.3}$$

with the block matrices defined as

$$\mathbf{K}_{\mathbf{u},\mathbf{u}} = \frac{\partial \mathbf{r}_{\text{equil}}}{\partial \mathbf{u}} = \int_0^L \mathbf{B}^{\mathrm{T}} \mathbf{C} \mathbf{B} \mathrm{d}x \tag{C.1.4a}$$

$$\mathbf{K}_{\mathbf{u},\widetilde{\mathbf{u}}} = \frac{\partial \mathbf{r}_{\text{equil}}}{\partial \widetilde{\mathbf{u}}} = -\int_0^L \mathbf{B}^{\mathrm{T}} \mathbf{C} \boldsymbol{\varepsilon} D'(\widetilde{Y}) \frac{\partial \widetilde{Y}}{\partial \widetilde{\boldsymbol{\varepsilon}}} \mathbf{B} \mathrm{d}x \tag{C.1.4b}$$

$$\mathbf{K}_{\widetilde{\mathbf{u}},\mathbf{u}} = \frac{\partial \mathbf{r}_{\text{regu}}}{\partial \mathbf{u}} = -\mathbf{M} \tag{C.1.4c}$$

$$\mathbf{K}_{\widetilde{\mathbf{u}},\widetilde{\mathbf{u}}} = \frac{\partial \mathbf{r}_{\text{regu}}}{\partial \widetilde{\mathbf{u}}} = \mathbf{M} + \ell^2 \mathbf{D} + \ell^2 \frac{\partial \mathbf{D}}{\partial \widetilde{\mathbf{u}}} \cdot \widetilde{\mathbf{u}} \tag{C.1.4d}$$

where

$$\frac{\partial D_{ij}}{\partial \widetilde{u}} = \int_0^L \frac{\mathrm{d}N_i}{\mathrm{d}x} \frac{\mathrm{d}g}{\mathrm{d}\widetilde{u}} \frac{\mathrm{d}N_j}{\mathrm{d}x} \mathrm{d}x \tag{C.1.5}$$

with

$$\frac{\mathrm{d}g}{\mathrm{d}\widetilde{u}} = -p \cdot d^{p-1} \frac{\partial d}{\partial \kappa} \frac{\partial \kappa}{\partial \widetilde{\varepsilon}} \frac{\partial \widetilde{\varepsilon}}{\partial \widetilde{u}} \tag{C.1.6}$$

Some remarks about the tangent matrix:

- Matrices $\mathbf{K}_{\mathbf{u},\mathbf{u}}$, $\mathbf{K}_{\mathbf{u},\widetilde{\mathbf{u}}}$ and $\mathbf{K}_{\widetilde{\mathbf{u}},\mathbf{u}}$ are the matrices already discussed by Rodríguez-Ferran et al. (2005).
- Matrix $\mathbf{K}_{\widetilde{\mathbf{u}},\widetilde{\mathbf{u}}}$ is modified by adding the derivative of the diffusivity matrix $\mathbf{D}$, which now depends on the non-local displacements $\widetilde{\mathbf{u}}$ because of the term $g(\widetilde{\mathbf{u}})$.

C.2 Two-dimensional problem

Finite element discretisation of the weak form of the equilibrium (see Rodríguez-Ferran et al. (2005)) and regularisation (Eq. (B.2.11)) equations leads to the two discrete weak forms

$$\mathbf{r}_{\text{equil}}(\mathbf{u}, \widetilde{\mathbf{u}}) := \mathbf{f}_{\text{int}}(\mathbf{u}, \widetilde{\mathbf{u}}) - \mathbf{f}_{\text{ext}} = \mathbf{0} \tag{C.2.1a}$$

$$\mathbf{r}_{\text{regu}}(\mathbf{u}, \widetilde{\mathbf{u}}) := -(\mathbf{M} + \ell^2 \mathbf{K}_{\text{BC}})\mathbf{u} + (\mathbf{M} + \ell^2 \mathbf{D})\widetilde{\mathbf{u}} = \mathbf{0} \tag{C.2.1b}$$

where

$$\mathbf{f}_{\text{int}} = \int_\Omega \mathbf{B}^{\text{T}} \boldsymbol{\sigma} \mathrm{d}\Omega \tag{C.2.2a}$$

$$\mathbf{f}_{\text{ext}} = \int_{\Gamma_t} \mathbf{N}^{\text{T}} \bar{\boldsymbol{t}} \mathrm{d}\Omega \tag{C.2.2b}$$

$$\mathbf{M} = \int_\Omega \mathbf{N}^{\text{T}} \mathbf{N} \mathrm{d}\Omega \tag{C.2.2c}$$

$$\mathbf{D} = \int_\Omega \nabla \mathbf{N}^{\text{T}} g(\widetilde{\mathbf{u}}) \nabla \mathbf{N} \mathrm{d}\Omega \tag{C.2.2d}$$

$$\mathbf{K}_{\text{BC}} = \int_\Gamma g(\widetilde{\mathbf{u}}) \mathbf{N}^{\text{T}} \boldsymbol{t}^{\text{T}} \boldsymbol{t} \boldsymbol{n}^{\text{T}} \nabla \mathbf{N} \, \mathrm{d}\Gamma \tag{C.2.2e}$$

with $\mathbf{N}$ the matrix of shape functions, $\nabla \mathbf{N}$ the matrix of shape function gradients and $\mathbf{B}$ the matrix of shape functions derivatives.

Linearisation of Equations (C.1.1) results in the tangent matrix

$$\mathbf{K}_{\text{tan}} = \begin{bmatrix} \mathbf{K}_{\mathbf{uu}} & \mathbf{K}_{\mathbf{u}\widetilde{\mathbf{u}}} \\ \mathbf{K}_{\widetilde{\mathbf{u}}\mathbf{u}} & \mathbf{K}_{\widetilde{\mathbf{u}}\widetilde{\mathbf{u}}} \end{bmatrix} \tag{C.2.3}$$

with the block matrices defined as

$$\mathbf{K}_{\mathbf{u},\mathbf{u}} = \frac{\partial \mathbf{r}_{\text{equil}}}{\partial \mathbf{u}} = \int_\Omega \mathbf{B}^{\text{T}} \mathbf{C} \mathbf{B} \mathrm{d}\Omega \tag{C.2.4a}$$

$$\mathbf{K}_{\mathbf{u},\widetilde{\mathbf{u}}} = \frac{\partial \mathbf{r}_{\text{equil}}}{\partial \widetilde{\mathbf{u}}} = -\int_\Omega \mathbf{B}^{\text{T}} \mathbf{C} \boldsymbol{\varepsilon} D'(\widetilde{Y}) \frac{\partial \widetilde{Y}}{\partial \widetilde{\boldsymbol{\varepsilon}}} \mathbf{B} \mathrm{d}\Omega \tag{C.2.4b}$$

$$\mathbf{K}_{\widetilde{\mathbf{u}},\mathbf{u}} = \frac{\partial \mathbf{r}_{\text{regu}}}{\partial \mathbf{u}} = -(\mathbf{M} + \ell^2 \mathbf{K}_{\text{BC}}) \tag{C.2.4c}$$

$$\mathbf{K}_{\widetilde{\mathbf{u}},\widetilde{\mathbf{u}}} = \frac{\partial \mathbf{r}_{\text{regu}}}{\partial \widetilde{\mathbf{u}}} = \mathbf{M} + \ell^2 \mathbf{D} + \ell^2 \frac{\partial \mathbf{D}}{\partial \widetilde{\mathbf{u}}} \cdot \widetilde{\mathbf{u}} - \ell^2 \frac{\partial \mathbf{K}_{\text{BC}}}{\partial \widetilde{\mathbf{u}}} \cdot \mathbf{u} \tag{C.2.4d}$$

where

$$\frac{\partial \mathbf{D}}{\partial \widetilde{\mathbf{u}}} = \int_{\Omega} \frac{\partial g}{\partial \widetilde{\mathbf{u}}} \nabla \mathbf{N}^{\mathrm{T}} \nabla \mathbf{N} \, \mathrm{d}\Omega \tag{C.2.5}$$

$$\frac{\partial \mathbf{K}_{BC}}{\partial \widetilde{\mathbf{u}}} = \int_{\partial\Omega} \frac{\partial g}{\partial \widetilde{\mathbf{u}}} \mathbf{N}^{\mathrm{T}} \boldsymbol{t}^{\mathrm{T}} \boldsymbol{t} \boldsymbol{n}^{\mathrm{T}} \nabla \mathbf{N} \, \mathrm{d}\Gamma \tag{C.2.6}$$

Some remarks about the tangent matrix:

- Matrices $\mathbf{K}_{\mathbf{u},\mathbf{u}}$ and $\mathbf{K}_{\mathbf{u},\tilde{\mathbf{u}}}$ are the matrices already discussed in Rodríguez-Ferran et al. (2005).
- Matrix $\mathbf{K}_{\tilde{\mathbf{u}},\mathbf{u}}$ is modified since $\mathbf{K}_{\mathrm{BC}}$ includes now the gradient activity control function g.
- Matrix $\mathbf{K}_{\tilde{\mathbf{u}},\tilde{\mathbf{u}}}$ is modified by adding the derivative of the diffusivity matrix $\mathbf{D}$ and of $\mathbf{K}_{\mathrm{BC}}$, which now depend on the non-local displacements $\widetilde{\mathbf{u}}$ because of the term $g(\widetilde{\mathbf{u}})$.

Bibliography

Armero, F. and K. Garikipati (1996). An analysis of strong discontinuities in multiplicative finite strain plasticity and their relation with the numerical simulation of strain localization in solids. *International Journal of Solids and Structures 33*(20-22), 2863–2885. doi: 10.1016/0020-7683(95)00257-X.

Bažant, Z. and M. Jirásek (2002). Nonlocal integral formulations of plasticity and damage: Survey of progress. *Journal of Engineering Mechanics 128*(11), 1119–1149. doi: 10.1061/(ASCE)0733-9399(2002)128:11(1119).

Bažant, Z. and B. H. Oh (1983). Crack band theory for fracture of concrete. *Matériaux et Construction 16*(3), 155–177. doi: 10.1007/BF02486267.

Belytschko, T. and T. Black (1999). Elastic crack growth in finite elements with minimal remeshing. *International Journal for Numerical Methods in Engineering 45*(5), 601–620. doi: 10.1002/(SICI)1097-0207(19990620)45:5<601::AID-NME598>3.0.CO;2-S.

Belytschko, T., J. Fish, and B. E. Engelmann (1988). A finite element with embedded localization zones. *Computer Methods in Applied Mechanics and Engineering 70*(1), 59–89. doi: 10.1016/0045-7825(88)90180-6.

Belytschko, T., Y. Krongauz, D. Organ, M. Fleming, and P. Krysl (1996). Meshless methods: An overview and recent developments. *Computer Methods in Applied Mechanics and Engineering 139*(1-4), 3–47. doi: 10.1016/S0045-7825(96)01078-X.

Belytschko, T., W. K. Liu, and B. Moran (2000). *Nonlinear Finite Elements for Continua and Structures*. Wiley.

Bourdin, B., G. A. Francfort, and J. J. Marigo (2000). Numerical experiments in revisited brittle fracture. *Journal of the Mechanics and Physics of Solids 48*(4), 797–826. doi: 10.1016/S0022-5096(99)00028-9.

Comi, C., S. Mariani, and U. Perego (2007). An extended FE strategy for transition from continuum damage to mode I cohesive crack propagation. *International Journal for Numerical and Analytical Methods in Geomechanics 31*(2), 213–238. doi: 10.1002/nag.537.

de Borst, R., J. Pamin, R. Peerlings, and L. Sluys (1995). On gradient-enhanced damage and plasticity models for failure in quasi-brittle and frictional materials. *Computational Mechanics 17*(1-2), 130–141. doi: 10.1007/BF00356485.

Francfort, G. A. and J. J. Marigo (1998). Revisiting brittle fracture as an energy minimization problem. *Journal of the Mechanics and Physics of Solids 46*(8), 1319–1342. doi: 10.1016/S0022-5096(98)00034-9.

Jirásek, M. (2000). Comparative study on finite elements with embedded discontinuities. *Computer Methods in Applied Mechanics and Engineering 188*(1-3), 307–330. doi: 10.1016/S0045-7825(99)00154-1.

Jirásek, M. and M. Bauer (2012). Numerical aspects of the crack band approach. *Computers and Structures 110–111*, 60–78. doi: 10.1016/j.compstruc.2012.06.006.

Jirásek, M. and T. Zimmermann (2001). Embedded crack model. Part II: combination with smeared cracks. *International Journal for Numerical Methods in Engineering 50*(6), 1291–1305. doi: 10.1002/1097-0207(20010228)50:6<1291::AID-NME12>3.0.CO;2-Q.

Mazars, J. and G. Pijaudier-Cabot (1996). From damage to fracture mechanics and conversely: A combined approach. *International Journal of Solids and Structures 33*(20–22), 3327–3342. doi: 10.1016/0020-7683(96)00015-7.

Mestre-Bellido, H. (2016). Damage initiation and propagation in non-local gradient models based on displacement smoothing. Master's thesis, Universitat Politècnica de Catalunya.

Miehe, C., L.-M. Schänzel, and H. Ulmer (2015). Phase field modeling of fracture in multi-physics problems. Part I. Balance of crack surface and failure criteria for brittle crack propagation in thermo-elastic solids. *Comput. Methods Appl. Mech. Eng. 294*, 449–485. doi:10.1016/j.cma.2014.11.016.

Moës, N., J. Dolbow, and T. Belytschko (1999). A finite element method for crack growth without remeshing. *International Journal for Numerical Methods in Engineering 46*(1),

131–150. doi: 10.1002/(SICI)1097-0207(19990910)46:1<131::AID-NME726>3.0.CO;2-J.

Nguyen, V. P., T. Rabczuk, S. Bordas, and M. Duflot (2008). Meshless methods: A review and computer implementation aspects. *Mathematics and Computers in Simulation 79*(3), 763–813. doi: 10.1016/j.matcom.2008.01.003.

Ortiz, M., Y. Leroy, and A. Needleman (1987). A finite element method for localized failure analysis. *Computer Methods in Applied Mechanics and Engineering 61*(2), 189–214. doi: 10.1016/0045-7825(87)90004-1.

Peerlings, R., R. de Borst, W. Brekelmans, and M. Geers (1998). Gradient-enhanced damage modelling of concrete fracture. *Mechanics of Cohesive-frictional Materials 3*(4), 323–342. doi: 10.1002/(SICI)1099-1484(1998100)3:4<323::AID-CFM51>3.0.CO;2-Z.

Rabczuk, T. (2013). Computational Methods for Fracture in Brittle and Quasi-Brittle Solids: State-of-the-Art Review and Future Perspectives. *ISRN Applied Mathematics 2013*, 38 pages. doi: 10.1155/2013/849231.

Rodríguez-Ferran, A., I. Morata, and A. Huerta (2005). A new damage model based on non-local displacements. *International Journal for Numerical and Analytical Methods in Geomechanics 29*(5), 473–493. doi: 10.1002/nag.422.

Simo, J. C. and J. Oliver (1994). A new approach to the analysis and simulation of strain softening in solids. In *Fracture and damage in quasibrittle structures*, pp. 25–39.

Simo, J. C., J. Oliver, and F. Armero (1993). An analysis of strong discontinuities induced by strain-softening in rate-independent inelastic solids. *Computational Mechanics 12*(5), 277–296. doi: 10.1007/BF00372173.

Simone, A., H. Askes, and L. Sluys (2004). Incorrect initiation and propagation of failure in non-local and gradient-enhanced media. *International Journal of Solids and Structures 41*(2), 351–363. doi:10.1016/j.ijsolstr.2003.09.020.

Simone, A., G. N. Wells, and L. J. Sluys (2003). From continuous to discontinuous failure in a gradient-enhanced continuum damage model. *Computer Methods in Applied Mechanics and Engineering 192*(41–42), 4581–4607. doi: 10.1016/S0045-7825(03)00428-6.

Sukumar, N., J. E. Dolbow, and N. Moës (2015). Extended finite element method in computational fracture mechanics: a retrospective examination. *International Journal of Fracture Mechanics 196*(1-2), 189–206. doi: 10.1007/s10704-015-0064-8.

Tamayo-Mas, E. (2009). Continuous-discontinuous models of failure based on non-local displacements. Master's thesis, Universitat Politècnica de Catalunya.

Tamayo-Mas, E. (2013). *Continuous-discontinuous modelling for quasi-brittle failure: propagating cracks in a regularised bulk*. Ph. D. thesis, Universitat Politècnica de Catalunya, Departament de Matemàtica Aplicada III.

Tamayo-Mas, E. and A. Rodríguez-Ferran (2013). A new continuous-discontinuous damage model: Cohesive cracks via an accurate energy-transfer process. *Theoretical and Applied Fracture Mechanics* (69), 90–101. doi: 10.1016/j.tafmec.2013.11.009.

Tamayo-Mas, E. and A. Rodríguez-Ferran (2015). A medial-axis-based model for propagating cracks in a regularised bulk. *International Journal for Numerical Methods in Engineering 101*(7), 489–520. doi: 10.1002/nme.4757.

Wells, G. N., L. J. Sluys, and R. de Borst (2002). Simulating the propagation of displacement discontinuities in a regularized strain-softening medium. *International Journal for Numerical Methods in Engineering 53*(5), 1235–1256. doi: 10.1002/nme.375.